Chapter 4
SiC MEMS devices

Silicon carbide microelectromechanical device development is currently a very active area of research with a primary focus on increasing the robustness of traditional silicon MEMS. Silicon MEMS has developed to a level of maturity in which several commercial ventures are deploying silicon technology into automotive and consumer electronics markets. A large knowledge base has developed into surface- and bulk-micromachined sensor types. This design expertise is being directly applied to sensor technology for harsh environment applications using SiC. This is accomplished because etch mask materials and etching techniques have already been developed that can be tailored to produce selective etching of SiC. These techniques can be linked together in a very similar fashion to silicon microfabrication, whether it be for surface- or bulk-micromachining of MEMS structures. This allows rapid development of SiC devices because the manufacturing concepts and design methodology can be readily applied. Hence, a large number of SiC MEMS sensor types have already been explored.

This chapter will first provide an overview of bulk- and surface-micromachining processes using SiC. This will be followed with a review of common MEMS sensor types as well as detailing research into using SiC to enhance traditional sensors. This will include a brief discussion of sensor design from the traditional application standpoint as well as specific considerations for deploying these sensor types into various harsh environment applications.

4.1 SiC MEMS processing

A generic SiC MEMS process flow is similar, although generally with fewer steps, than a generic IC process flow. Depending on the integration method, the MEMS process flow may start directly after the IC process flow or may start with the bare substrate. The primary differences between a MEMS process flow and IC process flow is the use of sacrificial etch layers to create free-standing structures and the use of deposited layers that are typically very thick compared to IC fabrication layers.

M.B.J. Wijesundara and R. Azevedo, *Silicon Carbide Microsystems for Harsh Environments*, MEMS Reference Shelf 22, DOI 10.1007/978-1-4419-7121-0_4,

As will be detailed more fully in Section 4.2, the free-standing structures are used to create mechanical devices sensitive to various measurand (*e.g.*, strain, acceleration, pressure). The thick layers used in to create these devices are needed to increase the sensor sensitivity by increasing the sensing surface or increasing the mass of the free-standing structure. The following sections schematically outline the process flow to create a generic SiC MEMS device starting with a bare substrate using two general classes of fabrication, bulk- and surface-micromachining.

4.1.1 Surface (thin-film) micromachining

Surface-micromachining is basically an extension of the IC fabrication process (Section 3.1.1). Alternating insulative and conductive layers are deposited to create mechanically connected electrical routing. The main difference is the inclusion of a sacrificial release layer that can be etched away without damaging the layers above or below, enabling creation of free-standing structures. The surface micromachining process begins by depositing a non-sacrificial insulating layer to allow selective electrical isolation of the subsequent electrical routing layer (Figure 4.1a). This isolation layer can be silicon dioxide although layers such as silicon nitride or aluminum nitride are preferred because of their higher degree of chemical inertness compared to silicon dioxide as well as closer match in thermal expansion rate to SiC, which is important for high temperature applications. If electrical contact to the substrate is needed, a lithography and etch step is used to open select vias through this non-sacrificial insulating layer prior to deposition of the subsequent routing layer (Figure 4.1b).

Next an electrically conductive layer is deposited (Figure 4.1c). This layer is typically a thinner version of the later device layer to ensure compatibility with that deposition step, which in this case would be LPCVD 3C-SiC. The conductive layer is likewise patterned to define the electrical routing layer needed for device functionality (Figure 4.1d). This etch process needs to have a high selectivity to the non-sacrificial insulating layer (rapid etch rate of the target layer but very low to zero etch rate to other exposed layers). As was discussed in detail in Section 2.5, SiC etch techniques are more commonly plasma-based. Hence, the very high selectivity achieved for silicon using wet chemical etching is not available for SiC. However, silicon carbide etching processes can be made reasonably selective to silicon dioxide [1] and aluminum nitride [2]. Silicon nitride is less favorable in this regard, although it has been used successfully [3].

Next a sacrificial layer is deposited (Figure 4.2e). Conductivity is not important; however, the film must be able to be deposited relatively thick (typically one to a few microns). Most importantly, the layer must have an etch chemistry that has very high selectivity to the device and routing layer as well as to the non-sacrificial insulating layer. Borrowing from traditional MEMS processing, silicon dioxide is typically the sacrificial layer of choice with vapor or liquid hydrofluoric acid as the preferred release etch chemistry. However, because of high chemical resistance of

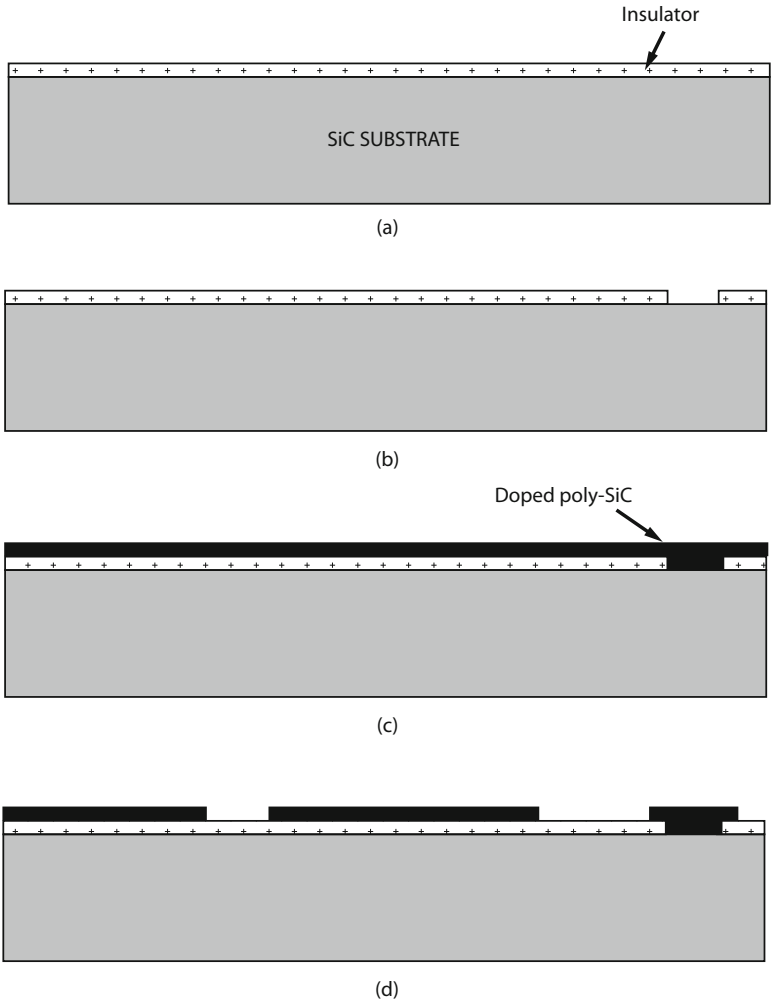

Fig. 4.1 Schematic of the first stages of fabrication of a single device layer surface-micromachined cantilever device with single electrical routing layer.

SiC compared to Si, a polysilicon layer is also a good option as a sacrificial material for SiC devices [6]. The sacrificial layer is typically patterned and etched to create via openings to the routing layer film (Figure 4.1f).

The sacrificial layer is followed with deposition of the SiC device structural layer (Figure 4.2g), which is again lithographically patterned and etched to define the device structure. The structural layer typically needs to be conductive, low-stress, and have a small stress gradient. This allows the layer to be shaped in a controlled way and maintain the desired gap dimensions around the structural device after the structure is released. Depending on its use, it may be important for the device

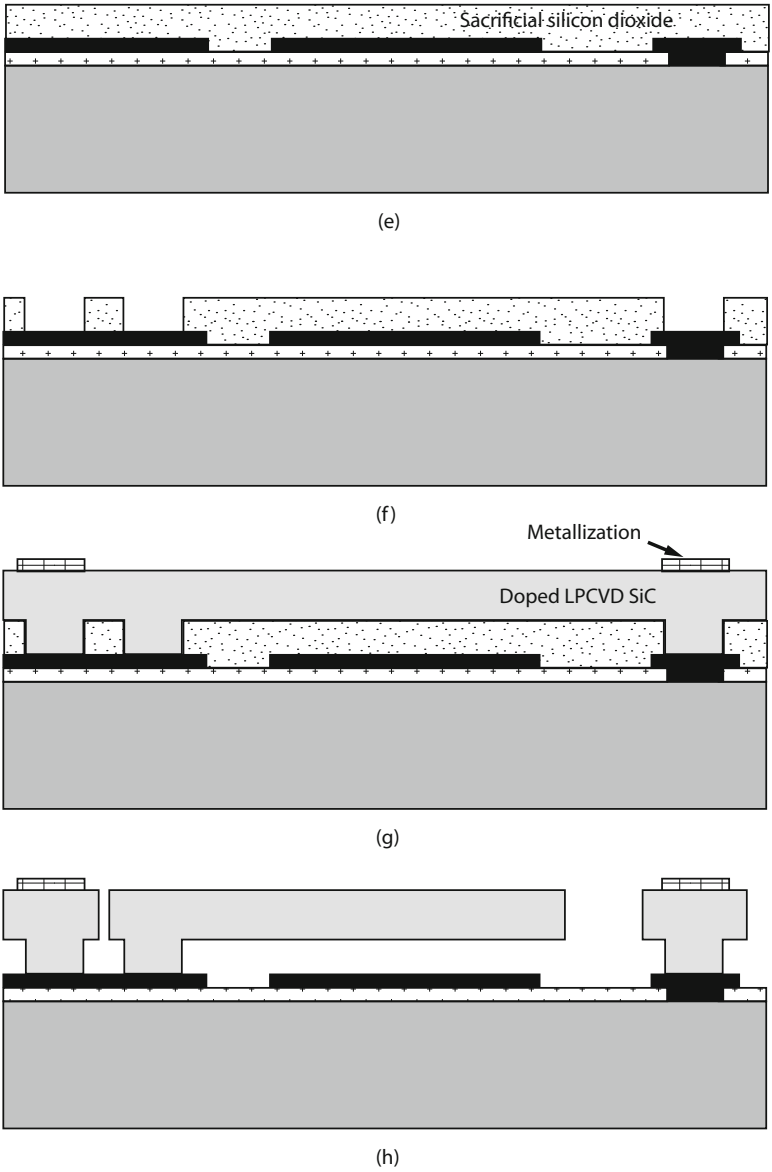

Fig. 4.2 Schematic of the final stages of fabrication of a single device layer surface-micromachined cantilever device with single electrical routing layer.

layer to also have proper ductility and fatigue characteristics. High stiffness allows for higher frequency operation. High yield strength prevents premature failure under shock or high acceleration events. The thickness of the device layer influences the resulting mass of the structure which is important for inertial sensing appli-

cations. Furthermore, in-plane sensing techniques will have signal amplitude that scales along with thickness, so the device layer thickness also influences the signal strength. Thickness also influences the stress developed during high-g acceleration. So proper design must consider all of these factors.

If needed for ohmic contact to wirebonds, a metallization layer will be deposited, lithographically patterned, and etched. Commonly the metallization is etched prior to patterning and etching of the device layer so that subsequent photoresist spinning does not need to coat and refill the deep trenches needed to penetrate the thick device layer. However, for simple structures in which the routing layer is omitted, the metallization can be deposited as a blanket film after the device layer is etched, using the device layer pattern to provide the necessary discontinuity in the metallization [4]. As was discussed in Chapter 3, Ti, Ni, and alloys with these metals are typically employed for this metallization layer, although other metals may be used depending on what corrosives the device will be exposed to during use.

Finally, the sacrificial layer is removed using a highly selective etchant (Figure 4.2h). Wirebonds are added to provide electrical connection to external power source and electronics if these are not integrated into the substrate.

Although it is not typically done, additional iterations of the insulating and routing layer deposition and patterning with additional interlayer insulator layers can be used to increase routing options depending on the electrical needs of a given sensor. Likewise, additional sacrificial and device layer pairs can be included in the overall MEMS fabrication flow to allow forming more complex structures including creating hinge structures or rotating gears. Fairly complex process flows have been successfully sustained for silicon MEMS fabrication [5]; however, this added complexity typically reduces yield or adds considerable cost. Therefore, many device design innovations in MEMS work to minimize the number of layers needed to fabricate the final structure.

4.1.2 Bulk micromachining

As was discussed in the previous section, device layer thickness can be a critical parameter in device design. Bulk-micromachining, where the substrate material is through-etched either to use the substrate as the device layer or a partial substrate etch is used to create a free-standing thin-film membrane, has become an equally important fabrication methodology in the manufacture of MEMS devices.

Because the substrate formation process is generally a high-temperature process not constrained to be compatible with other material layers, the resulting substrate fabrication process is optimized to create a high quality crystal with few defects and can be made with low stress. Additionally, the substrate is inherently thick compared to deposited films since it is created by slicing segments from a large boule of crystalline material (Section 2.2). Hence, substrates are generally hundreds of microns thick. Since selective etching processes have been developed for a wide range of substrate materials, including SiC, that are not high temperature, a bulk-

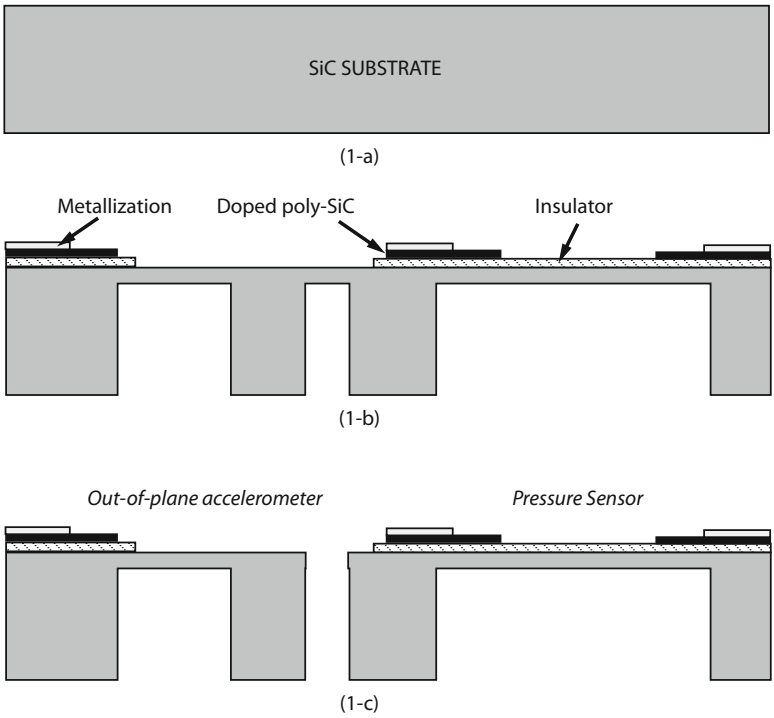

Fig. 4.3 Schematic of process flow to create bulk-micromachined cantilever and membrane devices using the substrate as a structural element. Additional detail is included to outline the basic process for incorporating piezoresistor elements into the structures for motion sensing.

micromachining process is attractive from a circuit integration perspective as well. (Integration issues will be discussed more fully in Chapter 6).

Figure 4.3 illustrates a generic process flow for bulk micromachining of a SiC substrate to create a free-standing beam and membrane. The process is comparatively simple and can be as simple as a single lithographic pattern and deep etch of the substrate; however, as is shown in the schematic flow, additional steps might be necessary to introduce other elements needed for sensing purposes. Etch characteristics, including selectivity to mask material and ability to etch high-aspect ratio trench structures, limits the usable substrate thickness and achievable gap dimensions, which can diminish some of the electrical signal gains achieved by having a tall structure. To achieve the necessary etch selectivity for bulk-micromachining, metal masking materials are typically required. Exposing the etch chamber to metal necessitates more frequent tool cleaning because the etch chemistry so slowly removes metal particles sputtered onto the chamber walls. Often fabrication facilities dedicate an etch tool to SiC etching using metal masks to prevent process cross-contamination. Furthermore, by etching completely through the substrate, the device now needs some encapsulation method to protect both sides of the substrate faces. (Encapsulation will be discussed in detail in Chapter 5).

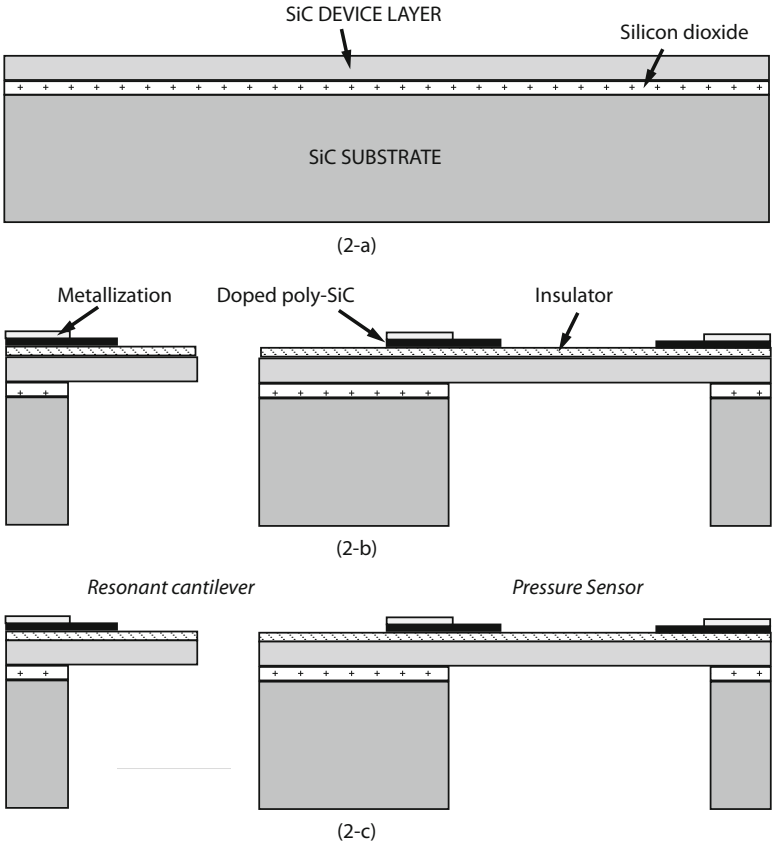

Fig. 4.4 Schematic of process flow to create bulk-micromachined devices by depositing a SiC thin-film layer and then etching the substrate up to the thin-film, which acts as the structural element. Additional detail is included to outline the basic process for incorporating piezoresistor elements into the structures for motion sensing.

Figure 4.3 illustrates a generic bulk-micromachining flow that utilizes a partial etch to create a free-standing membrane structure. The number of process steps is very small. In the case of the membrane (right side of Figure 4.3), additional structures will need to be fabricated on top of the membrane (such as thin-film piezoresistors) or onto a second wafer that can be be placed in close proximity to the membrane (such as a capacitor electrode) in order to detect membrane deflection. In order to sense pressure, the membrane must be subjected to a pressure differential, which necessitates isolating the frontside of the membrane from the back. This can be accomplished by embedding the substrate into another component to provide the necessary isolation or by creating a reference cavity behind the membrane by bonding another substrate below the etch pit. By continuing with the partial trench process and then patterning a through-etch region (Figure 4.3-1-b and -1-c, right side), it is possible to make a free-standing cantilever with a substantial end-mass.

This can be useful for inertial sensing because it allows some decoupling of the spring stiffness from the inertial proof-mass, increasing the flexibility of the design.

A common variation on bulk-micromachining of a membrane is to first deposit a thin-film membrane and then proceeding to a through-etch of the substrate to stop on the membrane (Figure 4.4). In order to get the desired selectivity for the stopping layer, a thin-film layer of silicon dioxide or aluminum nitride might be added under the SiC membrane film. In the case of silicon dioxide, the etch stop layer can be easily etched away selectively. Although this may not be necessary, silicon dioxide is not as robust a mechanical material so may be removed to minimize shifts in membrane characteristics over time.

4.2 Devices and operation in harsh environment

This section provides a review of state-of-the-art SiC sensors for harsh environment sensing. Harsh environment sensing covers essentially the same gamut of measurands as traditional commercial sensing: pressure, acceleration, strain, temperature, chemical composition, and characteristics of fluids such as viscosity or opacity. Each sensor type review will begin with a brief introduction into the general design methodology for the particular measurand. As needed, a brief introduction into the sensing method will also be outlined. Throughout, considerations of implementing these sensors in harsh environment conditions will be discussed.

4.2.1 Strain

Various structures — ship and spacecraft hulls, aircraft wings, pressure vessels, industrial piping — experience variable structural loads due to weight, expanding gases, or variations in temperature. For these type of structures, real-time monitoring of structural deformation either by monitoring peak dynamic load or by long-term monitoring of minute drift in shape (creep) can be used to signal scheduling preventative maintenance, remove the structure from active operation, or to restrict operation to a reduced-load operating condition (e.g., reducing process pressure to prevent structural failure). These structural changes can be monitored through the use of strain sensors mounted on the surface of the structure.

Strain is a useful metric of deformation and creep of a mechanical structure. The one dimensional measurement of engineering strain when the underlying strain field is constant or linearly varying with position is given by:

$$\varepsilon = \frac{\Delta l}{l_0} \tag{4.1}$$

This change in dimension can be measured purely as a change in length. Strain measurement techniques that measure the displacement over a fixed length (referred to

as the gauge length) that results from strain in a structure are referred to as extensometers. Extensometers are an indirect measurement of strain. This was originally a common method of measuring strain in macro-scale applications. However, these have been largely displaced by thin-film piezoresistive strain gauges (metal-foil gauges).

Some materials experience changes in electrical properties due to strain in the material. This effect is called a "piezo" response. Two common classes are piezoresistive and piezoelectric. Piezoelectric response is exhibited by certain materials such as quartz and aluminum nitride when the material is in a highly oriented crystalline form. Piezoelectric response of SiC films is very poor, so this mechanism will not be discussed in detail here, although the interested reader is directed to [7] for more information.

Most semiconductor materials exhibit a large piezoresistive response, including polycrystalline SiC [8]. Piezoresistivity is a change in electrical resistance with applied strain. The degree of piezoresistivity can be tailored somewhat by the type and amount of doping in the semiconductor. When strain is applied to a piezoresistor, the electrical resistance of the film changes because of the three-dimensional change in the structure due to Poisson coupling as well as an inherent change in resistivity due to the applied strain. Taking the example of a slender piezoresistive trace deposited directly onto a substrate that can experience mechanical deformation, the change in resistance is given by:

$$\frac{\Delta R}{R_0} = (1+2\nu)\varepsilon + \frac{\pi}{\xi}\varepsilon \tag{4.2}$$

where ξ is the resistivity of the film, ν is Poisson's ratio, π/ξ is the piezoresistance constant, and the subscript 0 refers to the unstrained state. Generally, it is desirable to have L be much larger than the width and strain gauge thickness should be minimized to ensure a uniform strain field through the entire thickness. Minimizing the thickness also prevents locally stiffening the structure, which can alias the resulting strain measurement [9]. The piezoresistance constant (gauge factor) for metal resistors such as Ni are on the order of 1 to 2. For semiconductors such as Si or SiC, it can be between 50 and 150 [8].

Typically, the measurement monitors the resulting voltage changes across the resistor while applying a known, constant current. It is certainly possible to use a frequency-based metric such as pairing the resistor with a capacitor to form a RC-tank, which has a frequency that is a function of resistance [10]. Because of electrical noise and thermal variations, it is also common to use multiple resistive elements in a Wheatstone bridge configuration to negate these variations [11].

Because of the very high accuracy with which changes in capacitance and frequency can be measured, strain using micromachined transducers is also measured using these techniques. These are extensometer devices. They may attempt to very accurately measure minute displacements or may involve mechanical structures for amplifying motion due to strain to increase the output displacement.

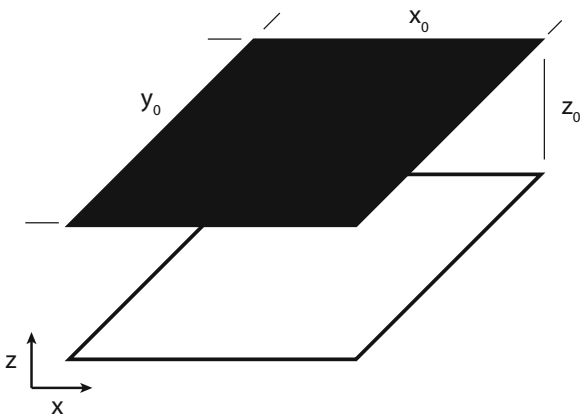

Fig. 4.5 Schematic of two square capacitor plates.

The capacitance between two parallel conductive plates (Figure 4.5) is given by the following equation:

$$C = \frac{\varepsilon x_0 y_0}{z_0} \tag{4.3}$$

where ε is the permittivity of the dielectric and is often written as some multiple of the permittivity of free space, ε_0 ($\varepsilon = \varepsilon_r \times \varepsilon_0$). The overlapping area of the plates is given by the lateral dimensions x_0 and y_0 while the distance between the plates is given as z_0. To allow freedom of motion, the dielectric is typically air or partial vacuum, thus $\varepsilon \approx \varepsilon_0$.

From this equation, it is seen that the capacitance can be varied mechanically by either changing the amount of overlapping area of the two plates:

$$\frac{\partial C}{\partial x} = \frac{\varepsilon y_0}{z_0} \tag{4.4}$$

or by changing the spacing between the plates:

$$\frac{\partial C}{\partial z} = -\frac{\varepsilon x_0 y_0}{z_0^2}. \tag{4.5}$$

For micromachined strain sensors, the intent is typically to measure either in-plane film stresses or to measure external strain applied to the substrate. In these cases, the capacitor plates are formed between beams cut out from the device layer. Example configurations are shown in Figure 4.6.

Changing the spacing between the plates (referred to as gap-closing mode, Figure 4.6b) is typically ten to one hundred times more sensitive than changing the amount of overlap area for the same initial gap dimension. In both modes, the change in capacitance is increased, hence the resolution is increased, if the initial gap dimension can be decreased or the surface area can be increased. The latter is accomplished by

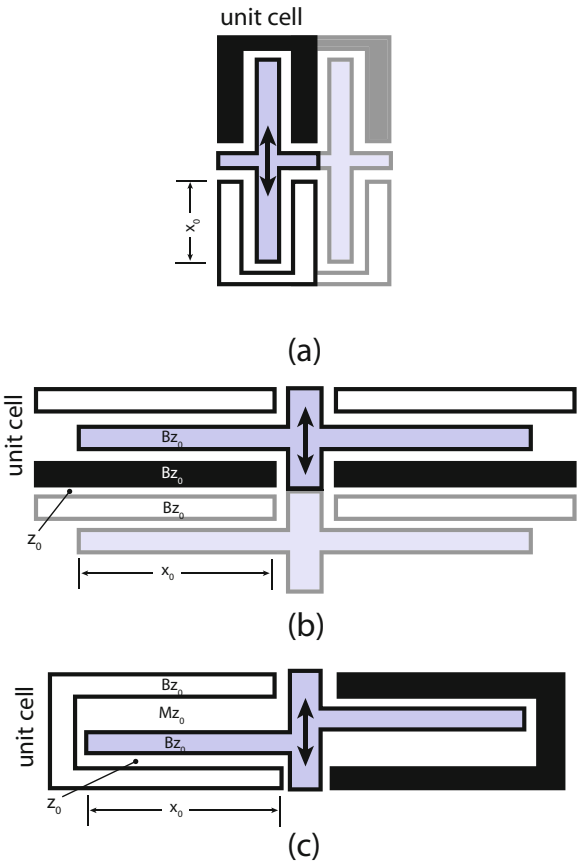

Fig. 4.6 Schematic of (a) lateral motion, interdigitated finger capacitor arrays and (b) gap-closing capacitor array utilizing independent plates on each side of the moving plate and (c) an offset-gap array when the stationary plates are not fully electrically isolated from each other.

increasing the device layer thickness and electrically connecting multiple plate pairs in parallel (plate arrays). The former though suffers from various limitations. In the gap closing mode, the linear region of response is limited to displacements less than about one tenth of the initial gap. This can severely limit the full-range strain measurable by the gauge. Both modes are limited by practical limitations in etching deep gaps, compromising the usable film thickness, which decreases the capacitor plate area. Also, very small gaps are more prone to contact each other either due to strain overload, external vibration (shock), or by the attractive force that forms in the capacitor when charge is applied.

For methods that use the change in overlap area (lateral mode), the most common topology is an array of interdigitated fingers, referred to as comb arrays (Figure 4.6a). For strain sensing, a chevron [4] or other lever mechanism is used to transform the small distortion due to strain into larger motion of the comb. Although the

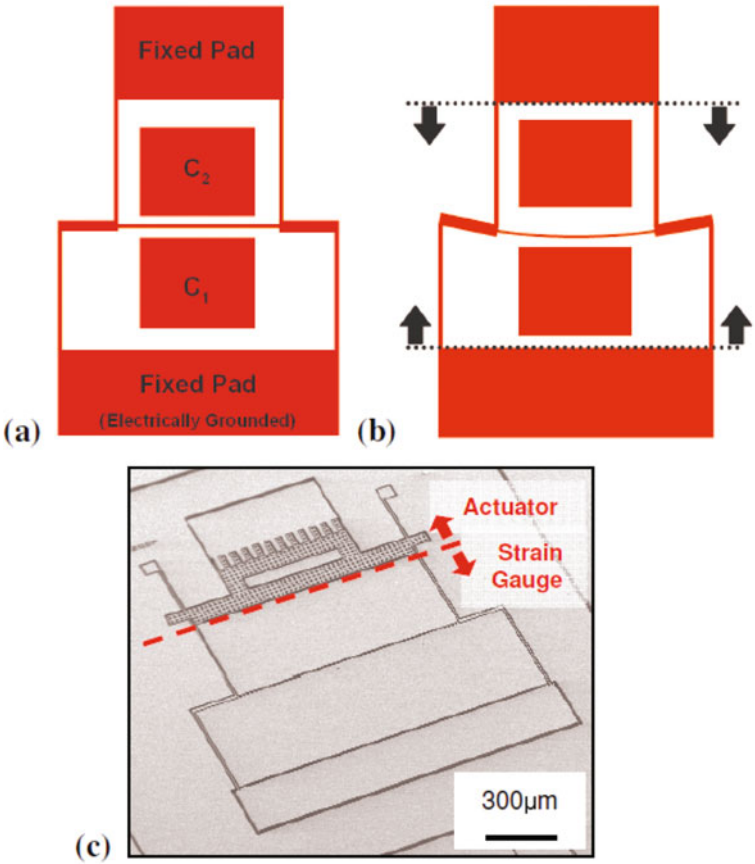

Fig. 4.7 [12] Schematic of four-point bending strain gauge design and SEM image of fabricated device coated with LPCVD SiC (©IEEE 2007), reprinted with permission.

lateral mode is linear over large displacements, the lever mechanism needs to be precise since any errors will also be amplified. Likewise, these amplifying mechanisms increase sensitivity to off-axis and temperature-induced strain. So all these factors need to be taken into account into the final design. Alternatively, mechanisms can be used to minimize degradation of on-axis signal while decreasing the influence of off-axis sensitivity, as was done by Jamshidi *et al.* [12]. In this case, an in-plane, four-point bending plate is loaded using slender tethers (Figure 4.7). The bending plate is part of a gap-closing capacitor, which is used to measure applied strain. The slender tethers along with having the bending plate longer than the fixed plate makes the structure insensitive to off-axis strain. This structure has been demonstrated as a SiC coated Si device fabricated from a SOI wafer and tested up to 370 °C.

Alternately, a resonant structure can be anchored between two points such that the anchors define the gauge length. Such a configuration will create a tension in

the resonant structure as a result of strain applied between the anchor points. Although any doubly-anchored structure can be used for this type of sensing, clamped-clamped beam and double-ended tuning fork (DETF) resonators are most common. Their resonant frequencies exhibit a high sensitivity to tension in the beam while being relatively insensitive to off-axis strain because of the large difference in structural compliance along the beam compared to perpendicular to the beam.

For a clamped-clamped beam with an attached proof mass, its resonant frequency of first bending mode can be written as follows:

$$f = \frac{1}{2\pi}\sqrt{\frac{198EI}{0.198\rho AL + kM_c} + \frac{4.85E\varepsilon}{0.198\rho AL + kM_c}} \tag{4.6}$$

where E is the Young's modulus of the beam, ρ is the density of the beam, I is the area moment of inertia, A represents the cross-sectional area of the beam, L is the beam length, M_c is the static mass of any structure attached to the beam such as a comb array, and k is a scale factor for this attached mass depending on location of attachment and the particular mode shape being excited during resonance. (For most practical applications the attached mass is at the center of the beam and the fundamental mode is used, in which case $k = 1$.) For details on how the constants are found for this mode shape, the interested reader is directed to [13] for details on theory of vibration. Typically MEMS resonators of this type range in frequency from 10s to 100s of kHz.

From Equation 4.6, one can calculate the change in frequency with applied strain. Normally, this result is non-dimensionalized by dividing the change in frequency by the nominal resonant frequency of interest:

$$\frac{1}{f_0}\frac{\partial f}{\partial \varepsilon} = \frac{2.425}{4.85\varepsilon_0 + 198I} \tag{4.7}$$

which, if the initial strain is zero, further reduces to

$$\frac{1}{f_0}\frac{\partial f}{\partial \varepsilon} = \frac{0.01225}{I} \tag{4.8}$$

Equation 4.7 can be used with ε_0 not equal to zero to account for residual stress in the device layer film by converting this stress into an equivalent strain using Hooke's Law. This implies that high residual tensile stress in the device layer film reduces the sensitivity of the resonator frequency to strain, which is consistent with experimental evidence.

Although this provides a means for strain to induce a change in frequency, the minute motion of the resonator needs to be detected in order to measure frequency. This is typically accomplished using gap-closing capacitive plates or lateral motion comb arrays. These are used not only because of their high sensitivity to motion, but also the capacitor can also be used to induce an in-plane force on the beam to excite and maintain the resonator vibration. From Equation 4.7, it is also clear that adding this mass comes at a cost of reducing the frequency to applied strain. So

again the overall design must weigh the benefits of the various topologies into the overall system requirements.

Initial work in harsh environment resonant strain sensing took conventional epitaxial Si strain sensors and coated them with a 30 nm thick LPCVD SiC coating [14]. These sensors were operated above 180 °C as well as were subjected to a potassium hydroxide (KOH) wet etch solution heated to 80 °C for 5 minutes. The coating was shown to protect the underlying Si. However, very high temperature operation (above 400-500 °C) requires converting this design to SiC due to Si softening.

A DETF strain sensor from polycrystalline 3C-SiC device layer has also been developed. Besides a change in device layer material, the work by Azevedo, *et al.* aimed to increase device robustness to high g-shock events [15]. A variation on standard DETF topologies was implemented to maintain the high transduction area of designs using comb sense arrays while preventing this suspended mass from causing failure due to stiction or excessive stresses in the structure. This is accomplished by relocating half of the comb drive structure between the tines to balance the mass symmetrically around the tines (Figure 4.8). Utilizing a square-wave drive oscillator topology [16], this 3C-SiC DETF resonant strain sensor achieved a comparable strain resolution to the standard comb-driven DETF topology built from an epitaxially-grown Si device layer (0.045 $\mu\varepsilon$ in a 10 kHz bandwidth, Figure 4.9). This 3C-SiC strain sensor has been successfully operated up to 600 °*C* in steam and subjected to 64,000 g shock without damage to the structure [3].

4.2.2 Pressure

Another common harsh environment sensor is a pressure sensor. SiC or SiC-coated Si pressure sensors are expected to find their greatest utility in monitoring gas or liquid pressure in industrial chemical applications. In addition, they will also find specialized use for space mission and medical applications.

Pressure sensing is typically accomplished by either monitoring membrane deflection under a pressure differential or by how pressure variation impacts the resonant frequency of a vibrating structure inside the variable pressure region. Membrane deflection is by far the most common pressure sensing method.

Membranes can be either round or rectangular. Maximum deflection occurs at the center of a symmetric membrane. For small deflections (less than half the membrane thickness), center-point deflection of a flat membrane under a static pressure differential is given by [17]:

$$\Delta z = \frac{pa^4}{64D} \tag{4.9}$$

for a circular membrane and

$$\Delta z = \frac{pa^4}{50D} \tag{4.10}$$

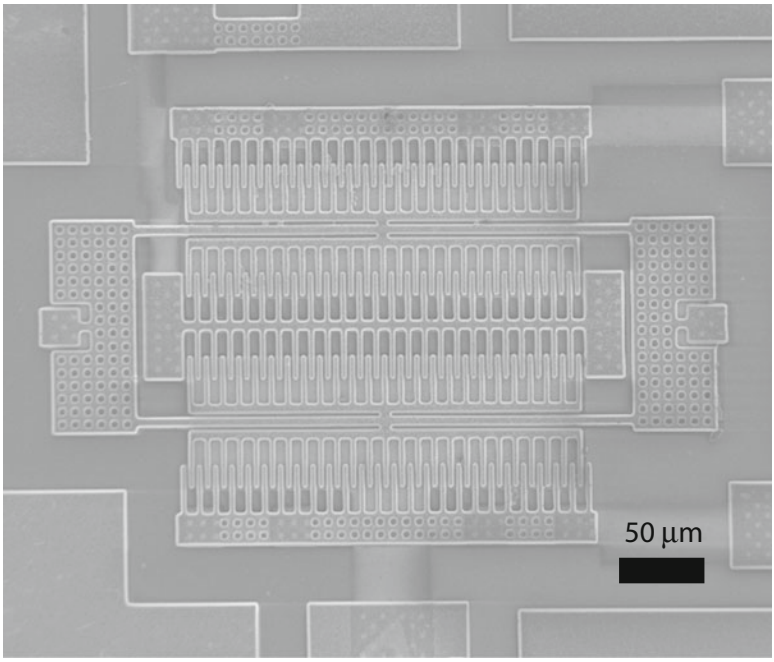

Fig. 4.8 [15] SEM image of a balanced double-ended tuning fork (BDETF) resonant strain sensor fabricated in a 4 mask process using LPCVD polycrystalline 3C-SiC as the device layer (©IEEE 2007), reprinted with permission.

for a square membrane, where a is either the radius or the half-length of the side of the square, p is the uniformly distributed pressure differential. D is the flexural rigidity and is related to the elastic modulus and plate dimensions:

$$D = \frac{Eh^3}{12(1-\nu^2)} \tag{4.11}$$

where h is the plate thickness and ν is Poisson's ratio.

As the deflection increases beyond half the membrane thickness, a cubic term response becomes significant due to the influence of shear stress in the membrane [18]. This can limit the full-range pressure measurable while maintaining output voltage linearity. In order to extend the linear response pressure range, a bossed membrane can also be used (Figure 4.10). For a circular bossed membrane, small deflections of the center boss as a function of pressure is given by [19]:

$$\Delta z = \frac{pa^4}{64D}\left(1 - \frac{b^4}{a^4} - 4\frac{b^2}{a^2}\log\frac{a}{b}\right) \tag{4.12}$$

where b is the radius of the boss feature. Although the boss stiffens the membrane

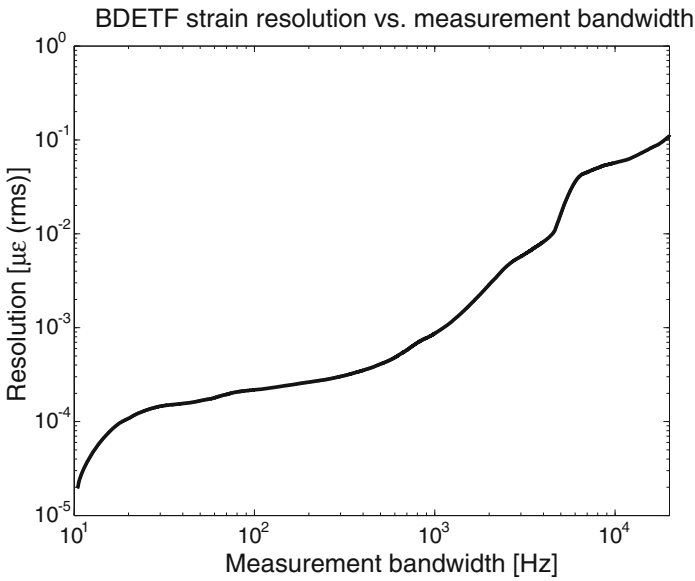

Fig. 4.9 [15] Experimental measurement of strain resolution as a function of measurement bandwidth for the 3C-SiC BDETF strain sensor (©IEEE 2007), reprinted with permission.

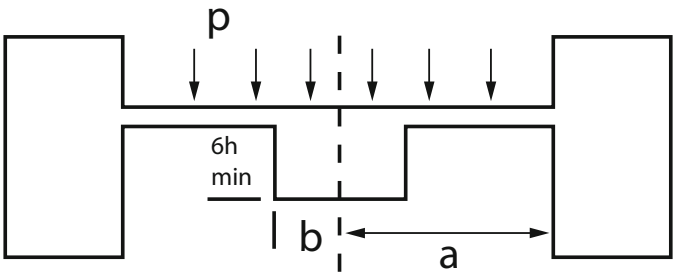

Fig. 4.10 Schematic of a bossed membrane diaphragm.

for a given size, it increases the linear response range for a given membrane size as well.

Small deflections of the membrane require sensitive measurement techniques. Semiconductor-based piezoresistive measurement techniques [11] convert strain in the resistor region into a change in electrical resistance, which can be used in a voltage sensing circuit to determine membrane deflection. Typically, a Wheatstone bridge configuration is used with the piezoresistors positioned so that strain increases resistance in one pair of resistors and decreases in another pair of resistors by positioning the resistor elements in tensile and compressive regions of the membrane, respectively. Peak radial strain occur at the perimeter of the membrane and can be related to pressure. From [18], this relationship for a flat membrane is:

$$\varepsilon_r = -\frac{3}{64}\frac{a^2 h}{D}p \tag{4.13}$$

Developing this sort of relationship allows depositing thin-film piezoresistors onto a diaphragm in order to accurately measure the pressure differential across the membrane.

Early pressure sensor work utilized doped 6H- or 3C-SiC as the piezoresistive element, although the diaphragm was either created by bulk-etching Si under the piezoresistive elements [21] or utilizing an SOI wafer to create a Si diaphragm. In this latter case, the 3C-SiC layer used to create the membrane could be selectively deposited on Si using an LPCVD process with methylsilane as the precursor gas and a fast carbonization step using ethane [22]. Deposition was carried out at 1150 °C. The Si device layer was thinned down to 200nm in part by thermally growing a 1400 nm thick silicon dioxide insulating layer over the device layer. This design utilized a bossed membrane and exhibited a 35mV/V sensitivity at 200 °C.

Current state-of-the-art SiC pressure sensors include depositing NiCr piezoresistive elements on a silicon dioxide layer to electrically isolate them from a n-type 3C-SiC film, which was grown on a Si substrate. Bulk chemical etching of the Si is used to form a free-standing SiC membrane [20]. A sensor constructed this way has been tested up to 400 °C with a full-scale pressure range of 500 kPa. It exhibits a temperature sensitivity of -0.16%/°C at 400 °C.

In order to make a pressure sensor capable of withstanding even higher temperatures and be less sensitive to corrosive environments that might etch NiCr, an all-SiC structure has also been developed. It was formed by first forming p-type 6H-SiC piezoresistive elements on a n-type 6H-SiC substrate. The substrate is then bulk etched using a photoelectric-enhanced chemical etch to form a 50 μm thick membrane [21]. This pressure sensor has been experimentally shown to exhibit stable pressure response up to 500 °C with a full-scale pressure range of 1000 psi. It exhibits a gauge factor temperature sensitivity of -0.11%/°C at 500 °C.

An alternate sensing technique is to use the membrane as one side of a gap-closing capacitor. In the case of a capacitive readout pressure sensor, typically the capacitor is formed by using the deformable membrane as one of the plates and placing it in relatively close proximity to a fixed electrode plate. A circular bossed membrane pressure sensor is well modeled using equation 4.14. In this case, a change in the gap distance, z, result in a change of capacitance. As a function of pressure, change in capacitance around the zero-deflection point is given by:

$$\frac{\partial C}{\partial p} = \frac{\pi p b^2 a^4}{64 D z_0^2}\left(1 - \frac{b^4}{a^4} - 4\frac{b^2}{a^2}\log\frac{a}{b}\right) \tag{4.14}$$

where the area is defined by the size of the boss, which is simply $A = \pi b^2$, where b is the radius of the boss. However, for a flat membrane pressure sensor, the actual change in z varies as a function of the radial position of the membrane. Hence, the actual change in capacitance calculation requires integrating the change in z with radial position. Using the standard deflection model for a clamped circular membrane under small deflection, one can determine a relationship between pressure

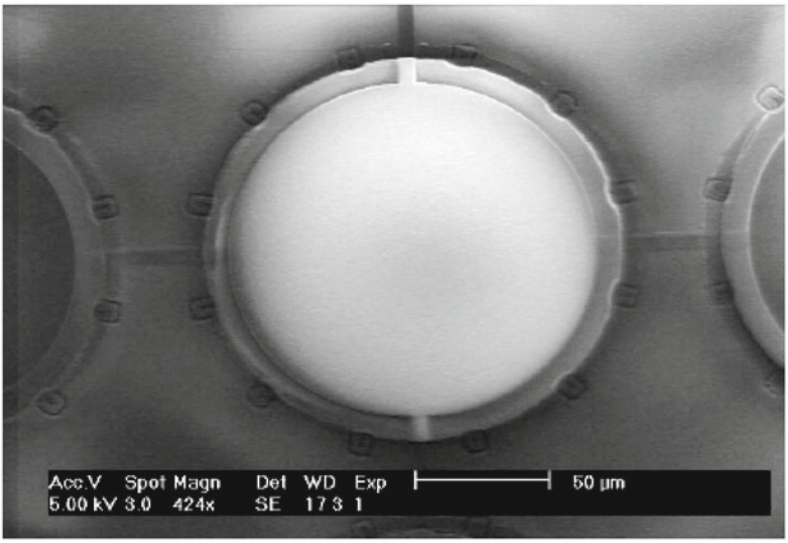

Fig. 4.11 [24] SEM image of a PECVD SiC pressure sensor (©IOP 2004), reprinted with permission.

and capacitance [23]:

$$C = \frac{\varepsilon a^2}{4h} \frac{(-ln(8\sqrt{hD} - \sqrt{p}) + ln(8\sqrt{hD} + \sqrt{p}))}{\sqrt{p}} \tag{4.15}$$

As is seen from equation 4.15, this relationship is in general non-linear, restricting operation to a relatively small pressure range if linear output is desired.

Surface-micromachined pressure sensors are of interest because the final sensor design is simpler since the backside of the diaphragm does not need to be encapsulated, and some bulk etching techniques are not compatible with integrated circuits. The mechanical quality of the sensor diaphragm is not as good as one formed from the substrate material because the substrate is a single-crystalline, very low-impurity material, whereas surface-micromachined diaphragms are typically a polycrystalline or amorphous film and may have non-uniform crystal growth or high residual stress. Process research aims to minimize these differences though because of the greater potential for integration with sense electronics and simplified packaging. An example of a surface-micromachined pressure sensor made from SiC was fabricated using PECVD a-SiC as the diaphragm material (Figure 4.11). Experimental measurements demonstrate a sensitivity of 3.2 pF/MPa and nonlinearity of 2% from 0.001 to 0.101 MPa for an array of 100 diaphragms that are 80 μm in diameter [24]. In this work, sputtered Al was used to form the fixed and moving electrode. The moving electrode is sandwiched between two SiC layers to prevent potential exposure of the Al to corrosive environments.

Because the deflection is restricted at the edges, the overall change in capacitance is significantly reduced without a boss structure. This in turn leads to the need for a very small gap, which can limit the ability of the pressure sensor to survive overpressure events. One way to overcome this is to introduce a dielectric coating over the stationary electrode, which prevents the two electrodes from shorting out when large pressures are applied. This technique has been successfully used for pressure sensing over a very wide range of pressures by purposely operating where the normal range of pressures causes the center of the diaphragm to contact the dielectric. After contact, increasing pressure leads to an increase in contact area. Although this leads to a number of nonlinear responses, experimental results show regions of decent linearity over a portion of the very wide range of pressures achievable with this type of sensor [25]. By having the critical gap dimension defined by a thin film dielectric instead of by etching means it can be manufactured with a highly controlled thickness down to nanometers. Furthermore, sensor output is increased because typically these dielectrics have a dielectric strength that is several to tens times greater than an air gap.

This touch-mode capacitive pressure sensor has been recently created out of an entirely SiC family of components [26]. The routing and diaphragm layers were formed from ammonia-doped 3C-SiC deposited using LPCVD (Figure 4.12). A Ni/Cr/Au stack was used as the high-temperature contacts. These sensors were tested up to 5 MPa (700 psi) static pressure. Although test chamber limitations prevented high-temperature testing at pressures above 100 psi (non-contact regime), a 172 μm diameter diaphragm demonstrated a sensitivity of 7.2 fF/psi at 574 °C. These sensors were successfully used for in-cylinder combustion pressure measurements on a test-bench setup.

Another method for pressure sensing in the vacuum regime is by monitoring the quality-factor (Q) of a resonator. In this case, by monitoring the frequency output of a resonator and watching either the 3dB width of the resonant signal amplitude peak or monitoring shifts in frequency due to Q variation, the pressure of the atmosphere in contact with the resonator can be determined. As the vacuum increases, the molecules around the resonator become less dense, leading to less collisions — the air damping decreases. Because air damping is an energy loss mechanism in a resonator, increased damping broadens out the resonant peak width in the frequency domain. Although this technique has been explored using silicon resonators, it has yet to be demonstrated using SiC.

The resonant structure for this method of pressure sensing can take a variety of forms, including the topologies laid out in Section 4.2.1. It can also take the form of a large diaphragm vibrating out of plane. Only, unlike in the previous diaphragm examples, this time a force generator is required to drive the diaphragm into the desired mode shape. This can be accomplished using a capacitive plate actuator or by depositing piezoelectric elements onto the membrane. Likewise, this technique has been applied to Si micro-sensors; however, it has yet to be demonstrated in SiC technology.

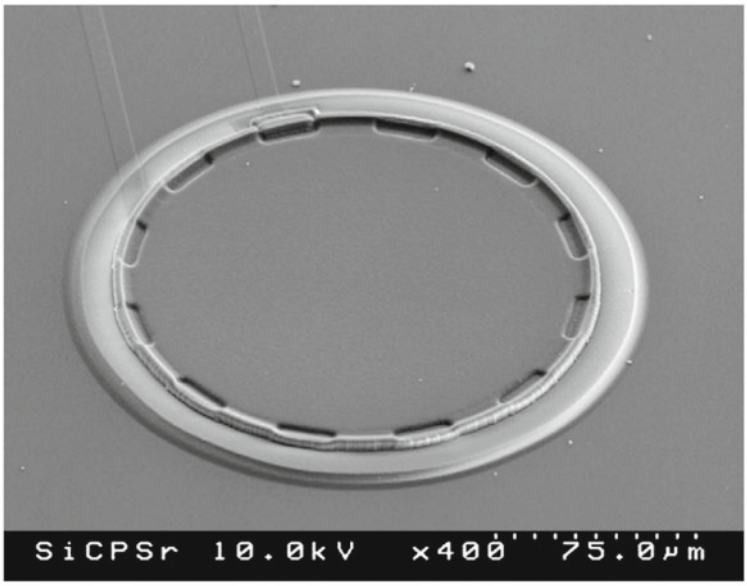

Fig. 4.12 [26] SEM image of LPCVD surface-micromachined pressure sensor element (©Elsevier 2008), reprinted with permission.

4.2.3 Inertial Sensing

Inertial sensing units are useful in motion sensing and navigation applications. Inertial sensing involves accelerometers, gyroscopes, and an accurate timing reference. Position information can be obtained by the double integration of acceleration with respect to time. So, if acceleration is known in three orthogonal directions along with a precise measurement of time, precise knowledge of position can be determined. Likewise, by knowing the rate of rotation about three orthogonal axes, precise orientation can be determined. By combining all of these components together, six degrees of freedom can be determined, creating a full description of a body's motion. Typical methods for determining acceleration and rate of rotation will be discussed along with specific examples of SiC versions intended for harsh-environment applications.

Accelerometers work by monitoring displacement of a well-characterized, movable mass (proof-mass) or by capturing the reaction force needed to hold the mass in place under an acceleration event. In the case of a displacement sensor topology, the mass is suspended such that the stiffness of the suspension is small in one direction but large in all other directions. Thus, the motion of the proof mass can be attributed to the component of acceleration that is aligned with the non-stiff direction of the suspension. In this case, resolution of the accelerometer is dependent on both the resolution of motion detection and the size of the proof mass since a larger mass will result in a larger deflection for the same suspension stiffness and acceleration.

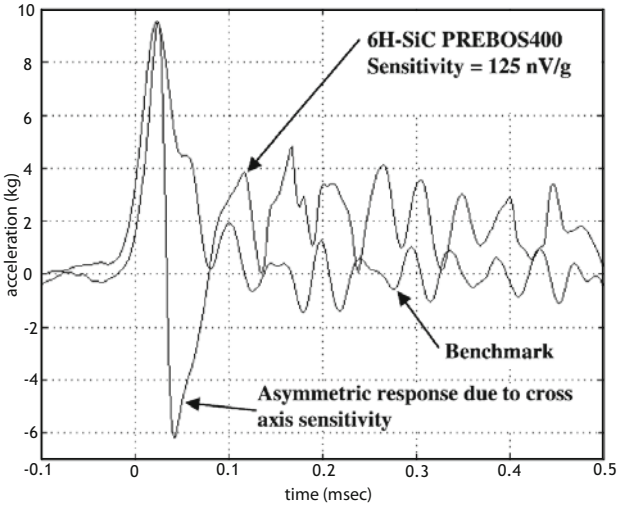

Fig. 4.13 [28] Comparison of out-of-plane membrane-based 6H-SiC accelerometer to a commercial high-g accelerometer (©Elsevier 2003), reprinted with permission.

Alternately, one can measure the reaction force needed to hold the proof mass in place. This force is directly proportional to the acceleration. A similar configuration for suspending the proof mass that limits proof mass motion to be preferential in one direction is often used so that the force sensor design can be optimized to measure a single-axis force. Force sensing accelerometers generally utilize the same phenomenon of varying tension in a vibrating element that is used in resonant strain sensors [27]. By including force actuators such as capacitive plates that can push back on the proof-mass until the detected displacement is reduced to zero, the voltage necessary to maintain a zero displacement condition becomes a measurement of the applied acceleration. By keeping the proof-mass stationary, nonlinearities are generally avoided and coupling to rotational acceleration during proof-mass motion is reduced.

SiC accelerometers to date have been of the displacement measurement type. Initial work used bossed membranes made from 6H-SiC substrates to detect out of plane acceleration [28]. Square and circular bossed diaphragms were fabricated and benchmarked against a commercial accelerometer (Endevco 7270-060 K). The sensors were well matched for accelerations below 8,000 g (Figure 4.13). However, above 40,000 g the SiC accelerometer showed non-linearities believed to be either due to residual stresses in the membrane or slight misalignment of the piezoresistive sense elements to the membrane. Although the boss increases the sensor sensitivity by increasing the proof mass, a flat membrane design was also developed because the boss tended to increase off-axis sensitivity as well by inducing a twisting motion.

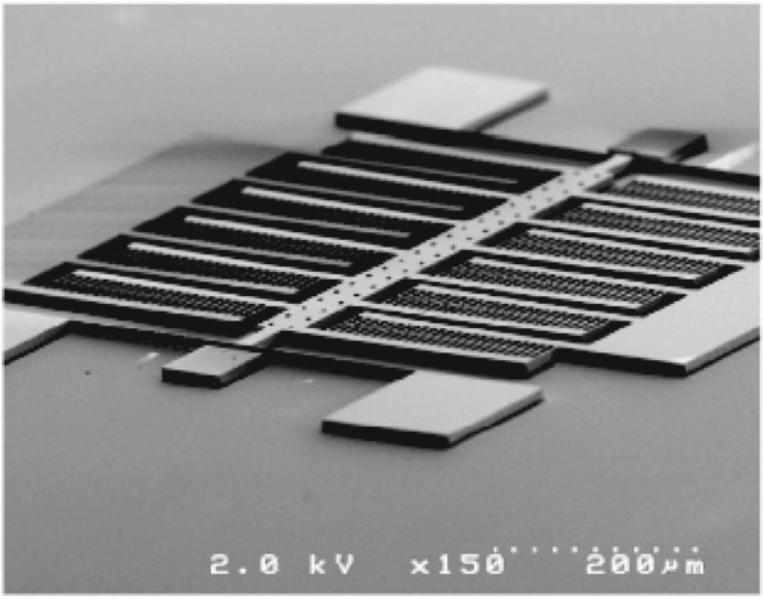

Fig. 4.14 [29] SEM image of an in-plane 3C-SiC accelerometer utilizing capacitive comb drives as the sense mechanism (©TTP 2009), reprinted with permission.

More recently, advances in strain gradient control and precision reactive ion etch micromachining have allowed development of in-plane single-axis SiC accelerometers. Utilizing large capacitive comb arrays as both part of the proof mass and the motion sensing mechanism, accelerometers created from LPCVD 3C-SiC have demonstrated a resolution of 350 $\mu g/\sqrt{Hz}$ at 1 kHz [29] (Figure 4.14).

PECVD a-SiC has also been used to fabricate in-plane and out-of-plane accelerometers [30]. Sensors made from a-SiC must also utilize a conductive layer for capacitive position readout. In this work, aluminum was used as the conductor (Figure 4.15). These sensors exhibit 1.8 fF/g and 2.3 fF/g sensitivities in the vertical and lateral directions, respectively. Because of the choice of materials and resulting low temperature deposition processes ($> 400\ ^\circ$C), these sensors are potentially Si CMOS compatible; however, the low deposition temperature makes PECVD films susceptible to creep if used for higher temperature applications.

Timing references do not need to use a mechanical element. A simple RC tank can be used as a timing reference; however, such a resonant system usually has high energy loss, which makes the drive circuitry power inefficient. By introducing a mechanical element into the oscillator circuit, a high frequency, high Q (tight frequency band) signal can be generated and used to keep track of elapsed time. The higher the precision that time is measured, the more accurate the position can be determined from rate of rotation and acceleration information.

Folded flexure resonators have been made by directly growing polycrystalline 3C-SiC on silicon dioxide on a Si substrate. Aluminum is used as the etch mask

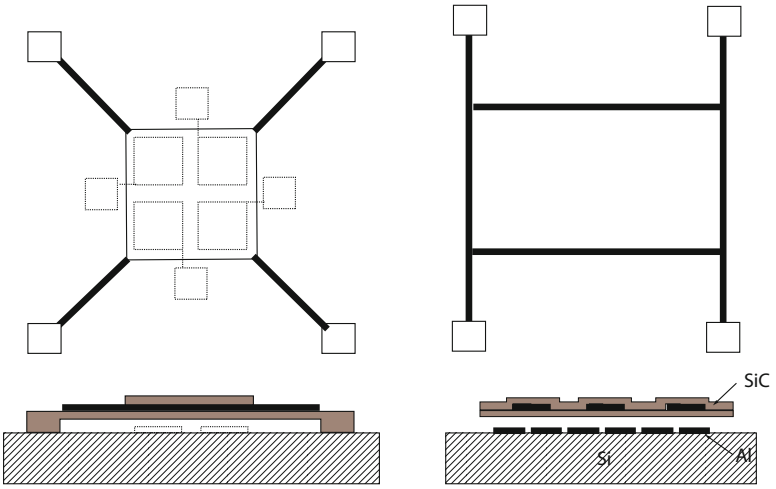

Fig. 4.15 [30] Schematic of layout for (left) out-of-plane and (right) in-plane accelerometers fabricated from PECVD a-SiC (©IEEE 2003), reprinted with permission.

material. This type of structure has an in-plane resonant frequency of 42.6 kHz with a 110 V actuation voltage [31]. These resonators were tested up to 900 °C. It was shown to exhibit significantly less shift in resonant frequency with temperature than an equivalent polysilicon resonator, presumably because of a higher sensitivity of Young's modulus to change in temperature for the polysilicon beams [32].

The DETF structure used as a strain sensor is also a potential timing reference. The resonant strain sensor operates at 218 kHz. However, it was only tested at atmospheric conditions, thus exhibiting a fairly poor Q of approximately 300-400 [14]. Even a simple cantilever structure can be used as a mechanical resonator. For instance a vertically-actuated SiC cantilever beam exhibited a resonant frequency of 1.5 MHz and a Q of 128 [33]. If these devices were operated under vacuum, significantly higher Q should be achievable.

A Lamé mode resonator array has also been demonstrated in polycrystalline 3C-SiC deposited using LPCVD. A fully-differential array of resonators exhibited a Q of 9,300 at a frequency of 173.5 MHz, operated in air [34]. The intended application was as a mechanical filter; however, it demonstrates higher frequency operation that could also be used for timing applications. A limitation of polycrystalline 3C-SiC resonators continues to be higher motional resistance. Even though very small capacitive gaps were formed using FIB in this particular example, motional resistance was still high for this resonator array. This is presumably because the sheet resistance in poly-SiC films is still significantly higher than other common materials, such as poly-Si. Nonetheless, as a basic resonator timing element, the Lamé mode resonator is a viable choice for SiC-based timing circuits.

Although the above resonators were all capacitively driven and sensed, thermally-actuated resonators have also been demonstrated (Figure 4.16). By patterning Pt or

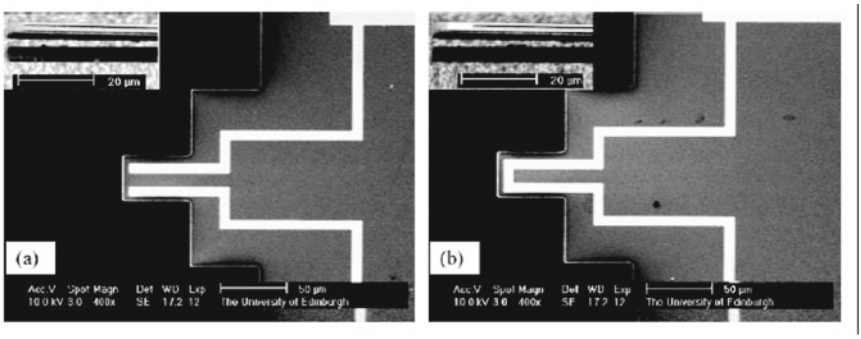

Fig. 4.16 [35] Two thermally-actuated SiC cantilever resonator designs. Pt is used as the electrode material (©Elsevier 2006), reprinted with permission.

Ni/Cr electrodes on hetroepitaxially-grown SiC cantilevers, resonant frequencies near 900 kHz have been achieved [35].

Gyroscopes are used to measure rate of rotation. This is accomplished most typically by a mass-in-frame configuration where a mass is vibrated in a direction orthogonal to both the axis of rotation of interest and the direction to which the frame is restricted to react. Monitoring either the position or reaction force generated by the frame due to a Coriolis acceleration that is generated during rotation gives a measurement of the rotation rate.

This type of single-axis gyroscope, using a variety of mechanical suspension and frame designs, has been implemented successfully in Si technology [36, 37, 38]. To date, no known micromachined gyroscope has been fabricated in SiC. With the successful implementation of strain sensors and accelerometers, SiC microfabrication has demonstrated all the necessary components to fabricate this type of device. Thus, it is just a matter of time before this last component for inertial sensing is realized in SiC.

Integrating the accelerometer and gyroscopes together in a fashion similar to newly emerging commercial Si-based inertial measurement units (IMUs) will be a challenge for the high-end temperature applications. The combined packaging of these devices will need to be developed using packaging ceramics that can survive the high temperature without generating large stresses in the package due to thermal expansion mismatch. Additionally, reduction of electrical interconnects is needed to improve the robustness of the packaged solution under these high temperature and potentially corrosive environments. These first-level packaging issues will be discussed more fully in Chapter 5. These complications need to be weighed against the process and design difficulty of requiring even higher degrees of monolithic integration of the IMU sub-components.

4.2.4 Chemical

There are a number of chemical sensors that utilize SiC films. Key advantages of SiC include chemical inertness and temperature stability without significant oxide growth or inter-metal diffusion. Being chemically inert allows the SiC films to be subjected to harsh chemical conditions without destroying the film. Minimal oxide growth and material property stability with temperature allows these sensors to maintain a higher level of stability than Si- or polymer-based sensors. Likewise, the low diffusion rate of metals into SiC maintain sensor stability when higher temperatures would otherwise suffer from metal migration into the ceramic films, changing their electrical characteristics.

Chemical sensors can be implemented using elements that are sensitive to adsorption of chemicals onto the surface. This includes capacitors, Schottky diodes, FETs, and surface acoustic wave (SAW) devices. In some instances SiC is not used directly as part of the sensing element, but may merely be a tough mechanical support that is tolerant to high localized temperature, particularly for use in micro-hotplate fabrication. In this case, the sense material is typically heated to stabilize the operating temperature or to improve sensitivity by promoting a chemical reaction.

Hydrogen is a common target chemical. By placing a catalytic metal (*e.g.*, Pt) onto a semiconductor surface, hydrogen atoms, either from a catalytic reduction of hydrogen molecules or hydrocarbons at the metal surface, diffuse through the metal to form an electrically-polarized layer at the metal-to-semiconductor interface [39]. When made part of a capacitor, this polarized layer lowers the flat band voltage. When part of a diode, it reduces the barrier height. By monitoring how the electronic device varies, the amount of hydrogen can be determined.

Oxygen atoms or nitric oxide molecules consume hydrogen, so tend to result in the reverse effect. Carbon monoxide reacts with oxygen, which in turn inhibits that oxygen from reacting with hydrogen. These competing mechanisms through their association with hydrogen can be sensed using hydrogen sensitive devices.

Two classes of SiC chemical sensors will be discussed. The first group are field effect devices, which use transistor of diode devices to detect the changes in electrical polarity due to hydrogen build-up. The second group do not use SiC to form the sensor elements but instead use it as a high-temperature, high-strength substrate for creating a suspended micro-hotplate to heat the sense elements.

4.2.4.1 Field Effect Devices

In 1997 metal-insulator-SiC (MISiC) sensor devices based on capacitors and Schottky diodes were tested [40]. These devices were constructed from 4H-SiC, and operating temperatures as high as 1000 °C were demonstrated with prolonged operation at 600 °C feasible. Response times were on the order of milliseconds. Additionally, interdiffusion of metal and insulator layers were studied. Response curves were generated for hydrogen, oxygen, and hydrocarbons.

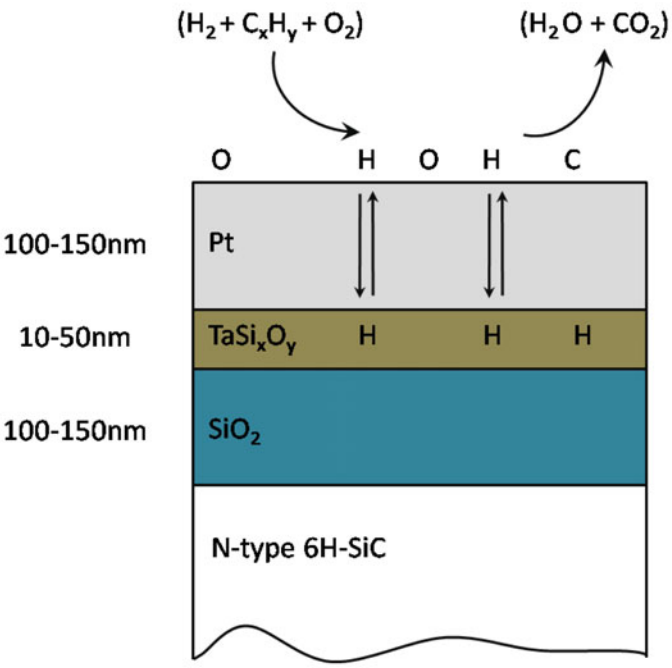

Fig. 4.17 [41] Schematic cross-section of a MISiC sensor that incorporates $TaSi_x$ as a buffer layer. This buffer layer interacts with the silicon dioxide layer to form a $TaSi_xO_y$ layer. (©Elsevier 1997), reprinted with permission.

Baranzahi *et al.* [41] further demonstrated 6H-SiC MISiC devices that incorporated a "buffer" layer between the metal and silicon dioxide (Figure 4.17). This buffer of 10 nm thick $TaSi_x$ improved the long term stability and response time of the sensors. These sensors were used to monitor hydrocarbons and were able to exhibit an output transition near a stoichiometric ratio in a simulated exhaust environment, which indicates complete combustion.

A MISiC structure that incorporated a LaF_3 buffer layer to increase the sensitivity to fluorine was developed in 1999 [42]. This structure was originally developed using a Si semiconductor layer. However, high temperature was needed for the catalyst and buffer layer to create the desired sensitivity. So the semiconductor layer was switched to SiC so that operation over 200 °C was feasible. This sensor was tested against F_2, HF, CCl_4, CH_4 and sensitivity to more complex fluorine compounds such as CF_3CH_2F to see if these compounds could be differentiated in the output. It was found that although there sensitivity was highest in the range of 200-330 °C, selectivity was not possible. But at 390 °C, selectivity was possible (Figure 4.18).

Work utilizing LaF_3 was then further extended to an array of MISiC sensors that utilized variations in metal catalyst (*e.g.*, porous Pt, Ir, Pt/Ir) to generate differentiating responses in a real exhaust environment. Figure 4.19 shows a schematic of the

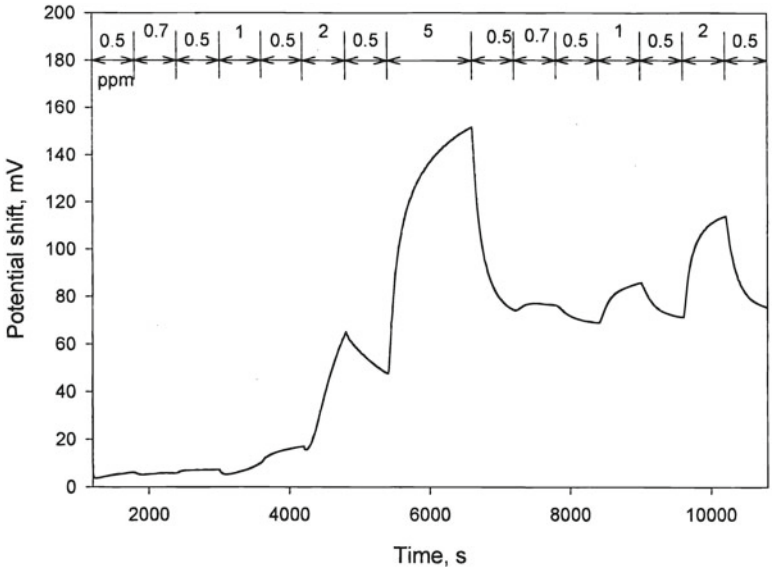

Fig. 4.18 [42] Response of a SiC gas sensor to HF at varied concentrations at 390 °C (concentration of HF in ppm is given in the upper portion of the graph). (©Elsevier 1999), reprinted with permission.

device utilizing a porous catalyst layer to increase the tri-interface regions as well as the response curves for such a device when exposed to an oxygen containing environment versus propane [43]. FETs became the device of choice because they combined the simplistic readout electronics of diode-based devices with the stability of capacitor-based devices since the FET devices also utilize a thicker oxide layer. This device is also easily adaptable to SiC, making it possible to operate these types of gas sensors at high temperatures either to improve sensitivity or because the application demands survival at elevated temperature, as is the case of in-cylinder combustion monitoring.

Although this array approach was shown to be somewhat successful, the general drawback of these types of sensors is the lack of a single sensor to a single chemical. So for practical implementation an array of sensors is likely needed to make the necessary distinction, which in turn requires a detection algorithm that can be quite complex depending on the models used [44].

4.2.4.2 Micro-hotplates

Micro-hotplates are useful for chemical sensing because control of the sense material temperature is advantageous in two main ways. First, actively regulating the sense element temperature to a constant level dramatically reduces thermally-induced drift or aliasing of the output signal. Second, in some cases by heating the

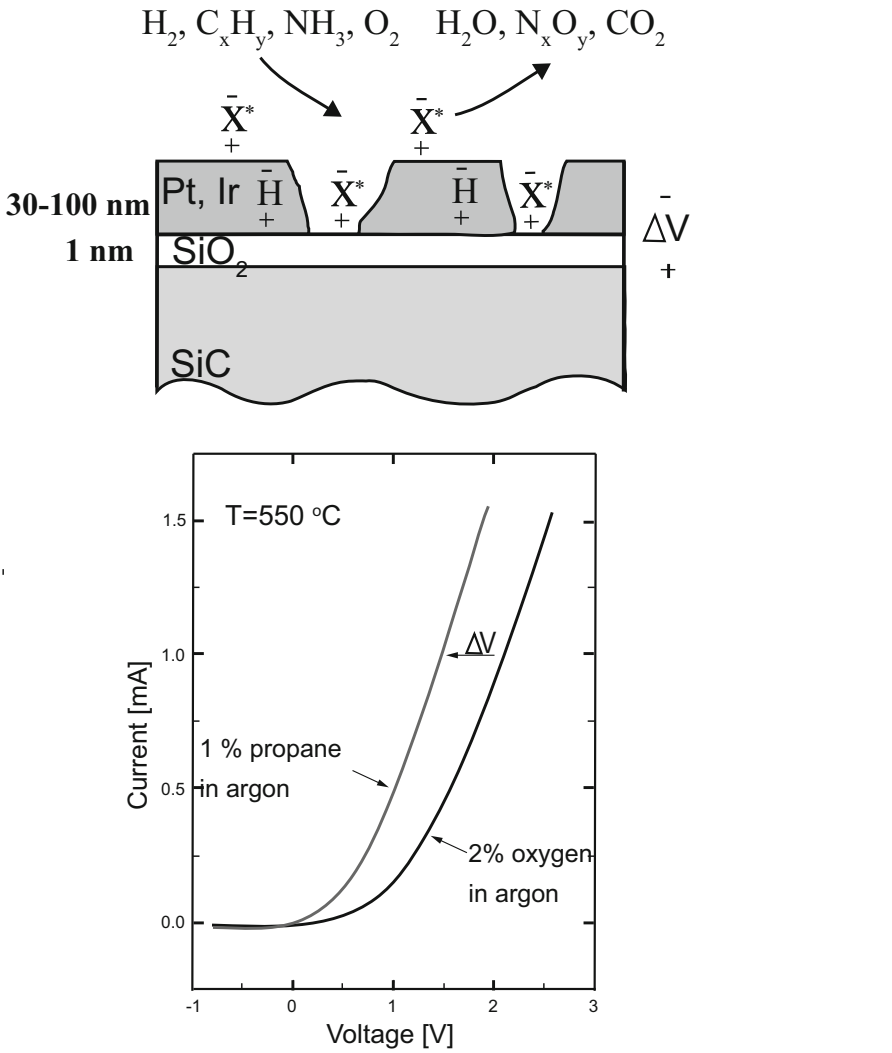

Fig. 4.19 [43] (a) Schematic of the MISiC sensor utilizing porous Pt and (b) response curve for this type of sensor when exposed to a propane or oxygen environment (©Elsevier 2001), reprinted with permission.

sense element to a high temperature leads to improved sensitivity to a given species or allows operating in a regime where response specificity among a selection of chemicals is greater.

Well-controlled, localized heating using resistive trace elements is typically achieved by creating a free-standing suspension on which the resistive elements are fabricated into and capped with metal oxides. SiC is a great candidate for these free-

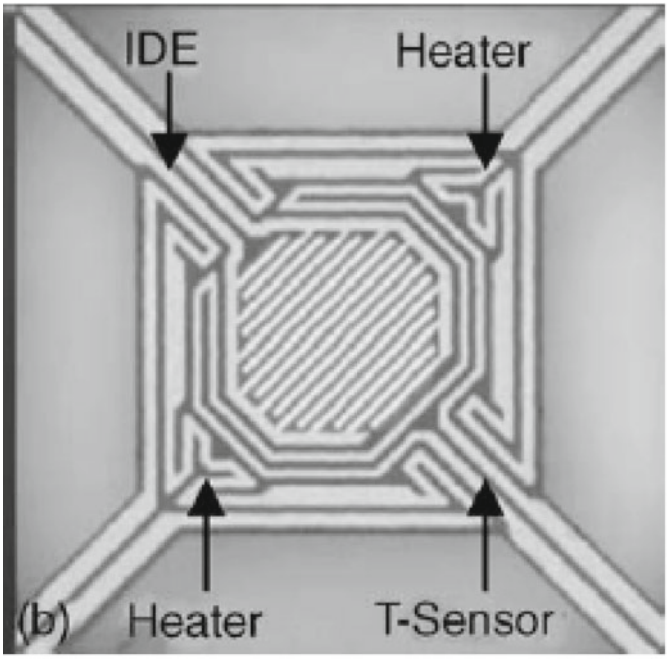

Fig. 4.20 [45] Microphotograph of micro-hotplate made on top of a 2 μm thick LPCVD 3C-SiC film (©Elsevier 2005), reprinted with permission.

standing suspensions because of the high mechanical strength, mechanical stability at high temperatures, and chemical resistance. Because silicon can be selectively etched with respect to SiC, these suspensions are typically deposited onto silicon substrates so that the silicon can simply be etched away under the SiC.

One example of such a design used a 2 μm thick LPCVD 3C-SiC film deposited on a Si substrate [45]. This film was covered with a 300 nm thick PECVD silicon oxide to isolate the catalyst from the substrate. Patterned Pt was used as the resistive heating element, temperature sensor, and inter-digitated electrode for chemical sensing. Finally, a second layer of PECVD oxide was deposited over the structure and gold was used to overcoat the bond pad regions (Figure 4.20). The micro-hotplate was able to heat up to approximately 500 °C using 300 mW, demonstrating the high temperature survivability of SiC. Continued work in this area should look at high ambient temperature chemical sensing. In this case, the micro-hotplate would likely need to be transitioned to a SiC substrate. It would also need to be operated at an even higher temperature than ambient to maintain a consistent chemical sensor temperature relative to changes in ambient.

4.2.5 Photo and Radiation Detectors

Light emitting diodes (LEDs) based on SiC were successfully commercialized in 1989 by Cree Semiconductor [46]. These LEDs have since been displaced by other wide-bandgap semiconductors because of low efficiencies of SiC-based devices. Reversing the light emitting process allows sensitive detection of light in the UV range. SiC photodetectors have been made on 4H- [47] and 6H-SiC substrates [48, 49]. These sensors have high efficiencies for UV wavelengths ($\sim$93% external quantum efficiency [47]) but are insensitive to visible wavelengths, allowing good selectivity.

SiC was investigated in the 1960s for use as a radiation detector, but again efficiencies were low; however, recently Stoken *et al.* have revisited SiC as a alpha ray and x-ray detector [50]. Higher purity levels of the SiC films that can be produced today have improved output efficiency compared to earlier attempts.

4.2.6 Temperature

Temperature sensing can be accomplished in a variety of ways. Generally, devices exhibit different degrees of temperature sensitivity. This is often something one wants to avoid. Temperature sensitivity in a device, such as a strain sensor or pressure sensor, can sometimes be counteracted by using an independent temperature sensor along with a model of the sensor response to temperature integrated into the sensor output electronics. Conversely though, isolating the strain sensor from strain essentially converts the sensor output to one that is solely a function of temperature. Therefore, optimizing temperature sensitivity instead of avoiding it can convert resistors, transistors, and resonators into usable temperature sensors.

Measuring resistance changes in a surface-micromachined thin film ceramic strip creates a low-complexity, compact temperature sensor. Termed thermistors, these temperature sensors have a long history. Many researchers have developed thermistors from SiC films and have studied the performance of the different polytypes with different dopant types and levels. In 1982, Nagai *et al.* demonstrated a SiC thermistor fabricated using magnetron sputtering onto an alumina plate [51]. These devices were trimmed to control the nominal resistance value prior to sealing inside a hermetic glass package (Figure 4.21). The resistance of these devices as a function of the inverse of temperature is shown in Figure 4.22. Thermistors have also been demonstrated using patterned metal electrodes on unintentionally doped 3C-SiC CVD wafers [52] as well as a high density array formed using magnetron sputtered SiC [53]. The array was specifically made into a linear array with regions as dense as 50 μm center-to-center spacing to characterize the thermal gradient at the liquid-vapor interface during evaporation (Figure 4.23).

In 1996, Casady *et al.* demonstrated a temperature sensor based on a 6H-SiC buried gate junction gate field-effect transistor [54] (Figure 4.24). The *pn* junction current was regulated using a series-series feedback network to prevent fluctuations. In this configuration, the *pn* junction voltage, v_d, was shown to have good sensitivity

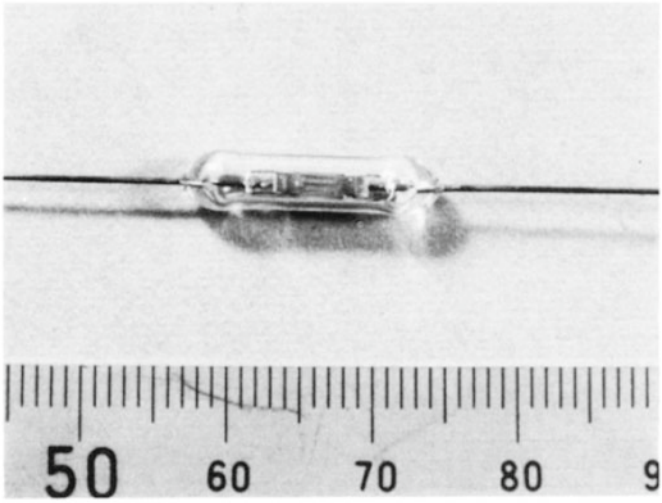

Fig. 4.21 [51] Hermetically sealed SiC thermistor (©IOP 1982), reprinted with permission.

(2.3 mV/°C) and excellent linearity from 25 °C to 500 °C. The sensitivity rapidly increased at -50 °C however, presumably because of carrier freeze-out in the diode.

Recently, a temperature sensor based on the optical signature of a SiC chip in a sintered SiC tube has been successfully used to accurately measure high temperatures up to 750 °C [56]. This sensor uses blackbody radiation, two-wavelength pyrometry along with Fabry-Perot laser interferometry to provide relatively fine temperature accuracy. Furthermore, this method uses the SiC chip as a free-space optic, which provides wireless operation. The use of a laser system is inherently bulky compared to a simple semiconductor resistor or JFET temperature sensor and requires, at least in the current configuration, that the laser be kept in a low temperature environment. This method though has promise in combustion engine or turbine environments where the high temperature environment is localized in the system.

4.3 Material aspect of harsh environment operation

This section will briefly discuss issues related to high temperature operation. Namely temperature-induced stresses will be discussed. Furthermore, control of stress gradient and its impact on being able to recreate certain devices that exist in Si technologies will also be discussed.

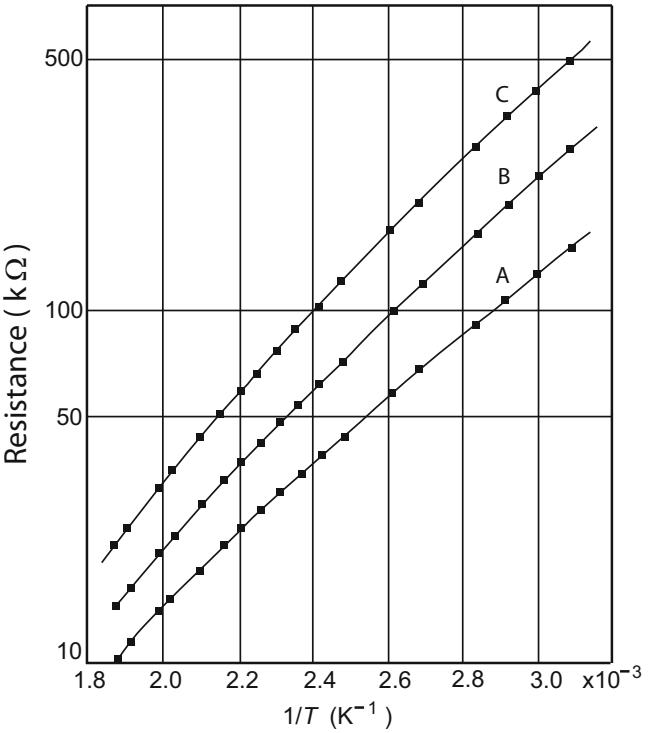

Fig. 4.22 [51] Temperature dependence of resistance of the SiC films deposited at various substrate temperatures with a particular electrode pattern: A 750 °C; B 700 °C; C 650 °C (©IOP 1982), reprinted with permission.

4.3.1 CTE of layers and effect

When operating temperatures can be hundreds of degrees Celsius over room temperature and dynamic temperature ranges can likewise be quite large, even small differences in how materials expand with increased temperature can be of critical importance. This is often captured as a coefficient of thermal expansion (CTE). CTE mismatch is a critical input in designing a sensor for harsh environment applications. Furthermore, CTE is generally not a linear function of temperature [57, 58, 59]. Figure 4.25 plots CTE values for SiC and Si based on a variety of deposition methods. It is interesting to note that the common CTE values listed in textbooks for Si and SiC do not apply to the same temperature range. In fact, near room temperature the CTE difference becomes very small.

In the case of a SiC double-anchored, flexural-beam resonator fabricated on silicon, the mismatch between the silicon substrate and the SiC device layer film leads to a higher frequency sensitivity to temperature than would be expected by elastic modulus softening of SiC alone (see Equation (1.13)). There also exists a region

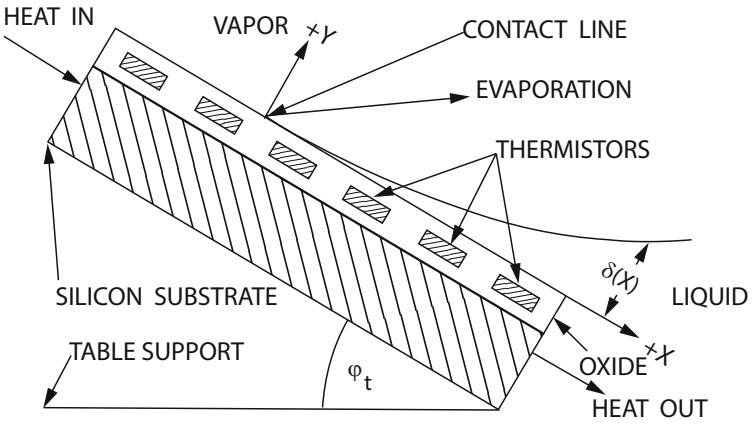

Fig. 4.23 [53] Schematic cross-section of thermistor array for use to generate a temperature gradient map at the liquid-gas interface during evaporation (©ECS 1989), reprinted with permission.

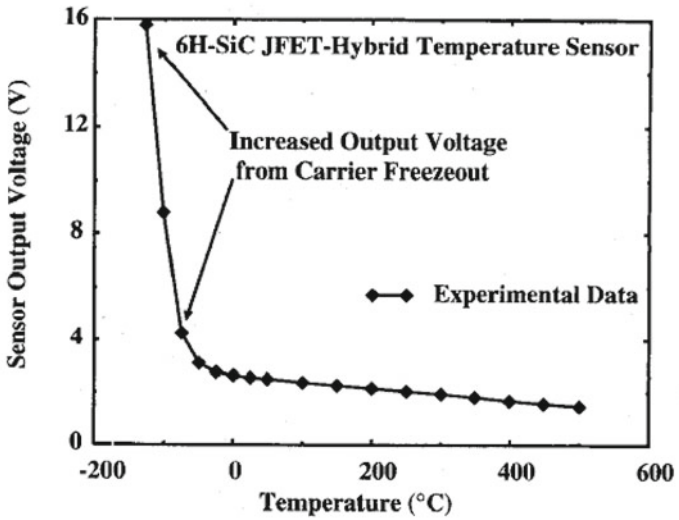

Fig. 4.24 [55] 6H-SiC junction gate field-effect transistor thermistor output voltage as a function of temperature (©Elsevier 1996), reprinted with permission.

near room temperature where the difference in CTE between Si and SiC is small, and the induced thermal strain (Figure 4.26) counteracts the strain due to stiffness softening [60]. In this regime of temperatures, frequency shift with temperature is very low. This provides a passive method capable of reducing thermal sensitivity for room temperature operation; however, at significantly higher temperatures, the sensitivity to temperature is amplified because of the CTE mismatch.

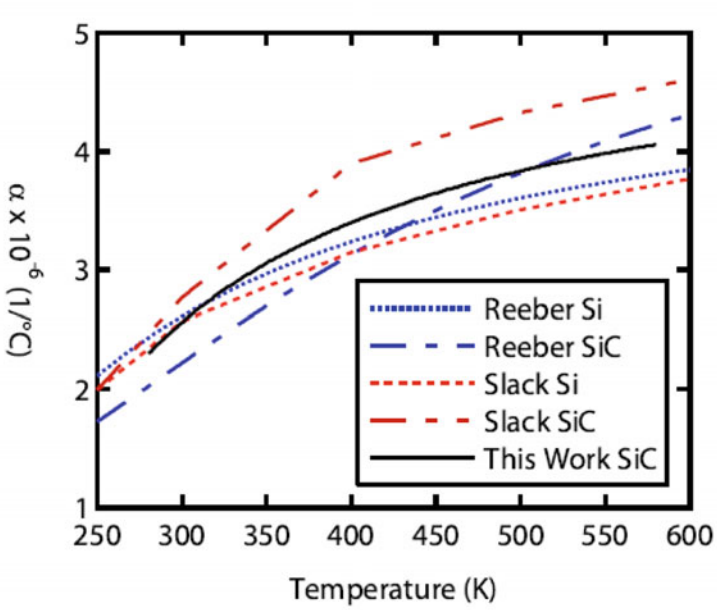

Fig. 4.25 [60] CTE as a function of temperature for 3C-SiC and Si as characterized by [57, 58, 59] and comparison to estimate of CTE for thin-film LPCVD 3C-SiC based on resonator response [60] (©IEEE 2009), reprinted with permission.

More extreme mismatches though tend to be detrimental to long-term survivability. Large cyclic loads are applied at the interfaces when materials with large CTE mismatch undergo large temperature changes. Therefore, whenever possible materials with closer CTE values should be the preferred design. For instance, it is better to use a-SiC compared to SiO_2 as an interlayer insulator between SiC or Si layers. For sustained high temperature operation, even the difference in CTE between the Si substrate, SiC device, and packaging layers can be problematic. Moving towards an all-SiC solution, utilizing a single-crystalline SiC substrate, alleviates the mismatch issue for high temperature operation. For very high temperature applications or applications that will continually cycle from room temperature to high operating temperatures, moving toward an all-SiC solution becomes a necessity for reliable long-term operation.

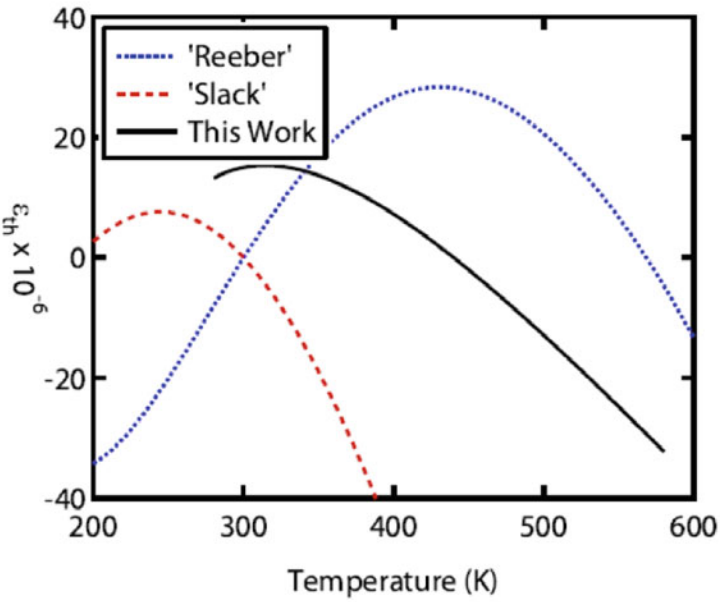

Fig. 4.26 [60] Thermal strain due to CTE mismatch between a silicon substrate and LPCVD 3C-SiC thin film based on literature for SiC and Si [57, 58, 59] and based on experimental measurements made using a double-anchored DETF resonator [15] (©IEEE 2009), reprinted with permission.

4.3.2 Stress gradient and stress relaxation

For mechanical elements of microsystems, stress and stress gradients impact device performance. In extreme cases, films may curl out of plane upon release (Figure 2.35), which for many applications would render the device unusable. The films may delaminate from the surface. Thus, stress and stress gradient can be limiting factors in achievable film thickness. Especially for electrostatic-based structures, thicker films are desired to increase signal strength since for an in-plane operated structure, the forces generated along with the spring constant scale linearly with thickness as does the device mass. For example, if operating an in-plane resonator then increasing the thickness results in essentially no change in frequency or drive voltage; however, capacitive coupling to the sense electrodes also scales upwards.

As has been discussed previously, the mechanical properties of silicon carbide films are very stable with temperature. This is one of the reasons why it is a leading candidate material for harsh environment applications. But this also makes it difficult to anneal out a significant level of stress [61, 62]. With silicon dioxides

and polysilicon layers, annealing often has a significant impact even when done at moderate temperatures. Annealing can be enough to reduce issues with stress or stress gradients. Silicon carbide has benefited in recent years by development of alternate methods of tailoring the mechanical properties. Tailoring the doping level, pressure, and flow of gases during deposition can be used to tune the stress. But for very thick films, often it is the variation in grain growth through the thickness that create a stress gradient. So work to likewise deposit with a gradient in gas flow or dopant concentration throughout the deposition has been able to create lower gradient films [63].

There still are device topologies from silicon micromachining that would be difficult to implement as is using SiC because they require a very long free-standing structure, requiring near-zero stress gradient. There is additional work to develop more strain gradient tolerant structures. By re-thinking some of the existing topologies in terms of anchor placement and how the structure folds upon itself is seen as an area of development that would be beneficial for SiC MEMS.

Epi-layer SiC or wafer-bonding of single-crystalline SiC to create SiCOI can create device layer films that are nearly stress free; however, this restricts the available topologies in terms of creating electrical routing layers or maintaining thermal budget if trying to integrate SiC electronics onto the same substrate as the MEMS device is important. So some solutions for the device realization standpoint need to be reviewed in the context of the overall system since they may limit options later in the system design.

4.3.3 Design for high g-shock survivability

Some level of shock survivability is usually considered as part of a commercial MEMS sensor mechanical design, from intentional accelerations expected in the field to accidental events such as dropping the sensor from a table. Although MEMS, due to their low inertia, are innately robust to moderate g-shock, certain harsh environment applications such as munitions monitoring require surviving shock events of 100,000 g or more. SiC has a favorable stiffness to weight ratio and good yield strength, but at these very high shock levels, more traditional designs may need to be modified to ensure device survivability. To highlight how design can be used to improve shock survivability, an example of how a SiC comb-driven double-ended tuning fork (CDDETF) resonant sensor is modified for high g-shock survivability will be discussed [15].

CDDETF resonators are commonly used in MEMS sensor applications and utilize electrostatic comb arrays for drive and sense of tine deflection (Figure 4.27a). The comb-array provides a higher transduction constant (due to increased capacitor surface area), which does not vary with the magnitude of tine excitation (minimizing distortion of the output signal). In addition, air damping is less for a comb array than for a gap-closing capacitor array of equivalent transduction efficiency. Thus, even though the added mass of the comb array decreases the resonator sensitivity

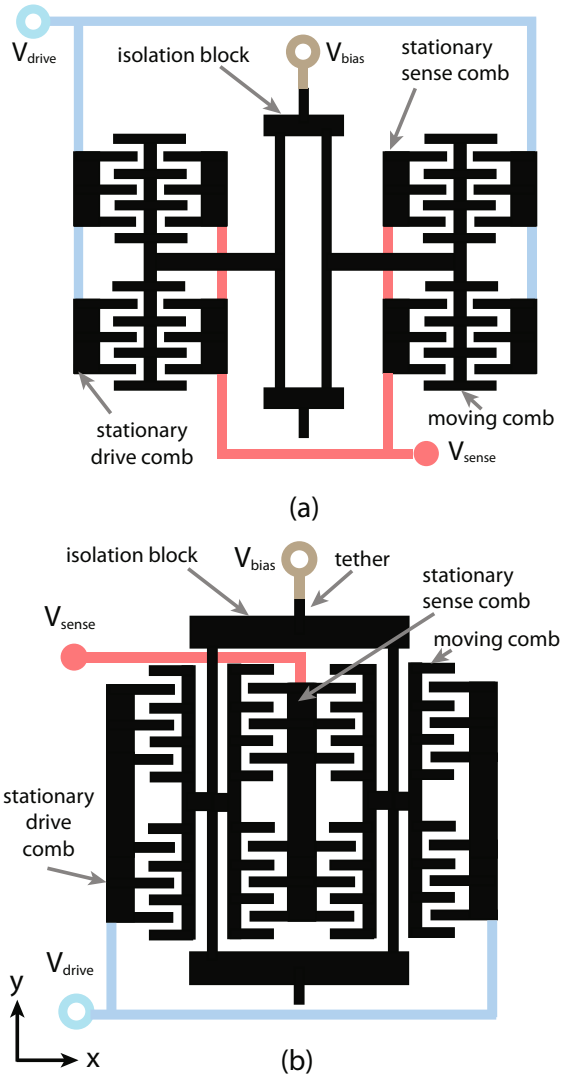

Fig. 4.27 [15] Schematics of (a) standard comb-driven double-ended tuning fork (CDDETF) resonator and (b) balanced-mass double-ended tuning fork (BDETF). (©IEEE 2007), reprinted with permission.

to applied strain or force [64], this is often tolerated because of the superior electrical characteristics achieved with the electrostatic comb array. This large structure is suspended far from the resonating tine and is detrimental to high shock survivability. It leads to a structure that is susceptible to deflection under shock, and the resulting load it creates on the tine and anchors cause high local stresses on other portions of the structure.

There are two primary modes of failure due to shock in MEMS: fracture and stiction. Preventing fracture, obviously, requires management of strains generated during a shock event. Stiction can occur either between the device layer and the substrate or, as is much more common, between the stationary and moving comb fingers of the capacitive comb array. Hence, to prevent stiction, it is also important to limit deflection during a shock event.

By folding the sense portion of the comb array between the tines, the long lever of the CDDETF structure is eliminated. The moving portions of the sense and drive comb arrays are now placed symmetrically around the tine, creating a balanced-mass comb-driven double-ended tuning fork (BDETF) topology (Figure 4.27b). To facilitate folding the sense comb array between the tines of the BDETF without significantly reducing the transduction area of the comb array compared to the CDDETF, the tine length is increased by 50% over the CDDETF design. Since the primary flexural mode resonant frequency and frequency sensitivity to applied strain of a clamped-clamped tine is constant for a given tine width-to-length ratio, the width of the BDETF tine is proportionally increased so as to maintain the same resonant frequency and sensitivity. In order to fit one half of the comb array between the tines requires widening the isolation block significantly over the CDDETF configuration. It is possible that widening the isolation blocks that connect the tines to the substrate anchors may increase anchor loss compared to the CDDETF; however, fluidic damping, not anchor loss, is the limiting factor in achievable Q for a resonator operated in air, which is how the original design is intended. Thus, changing the resonator to a BDETF does not diminish the strain sensor transduction performance while theoretically improving the g-shock survivability of the sensor over the standard CDDETF.

Simulations were conducted using ANSYS at 10,000 g, 50,000 g and 100,000 g in three directions: out-of-plane (z-axis), in-plane parallel to tines (y-axis), and in-plane perpendicular to tines (x-axis). Fracture failure was determined to occur first for both designs under z-axis acceleration. SiC is assumed to have a fracture strain limit of 0.17% based on literature review of CVD SiC films that examined comparably sized features. Therefore, the CDDETF is fracture-limited to 70,000 g, compared to 94,000 g for the BDETF design. The other mode of failure is stiction. For this type of structure, contact occurs either with the substrate or with the moving comb array fingers contacting the stationary fingers. Contact with the substrate will occur under 23,000 g z-axis acceleration for the CDDETF; whereas, the BDETF can survive 150,000 g based on extrapolation of the simulation data. Comb finger contact occurs at 93,000 g y-axis acceleration for the CDDETF while the BDETF reduces deflection in the y-axis by 98%.

By understanding the failure modes of the device structure along with general design constraints of the sensor enables sensor redesign that increases shock survivability considerably (in this example as much as four-fold). With careful design considerations, these gains can be made without significant compromise to sensor performance. Sometimes, as in this particular example, understanding the dominant loss mechanisms in the device allows improving shock survivability without reducing sensor sensitivity.

References

1. Gao D, Wijesundara MBJ, Carraro C, Howe RT, Maboudian R (2004). Transformer coupled plasma etching of 3C-SiC films using fluorinatedchemistry for microelectromechanical systems applications. Journal of Vacuum Science Technology B 22(2):513–518
2. Jones DG, Pisano AP (2010). Aluminum nitride as a masking material for the plasma etching of silicon carbide structures. IEEE 23rd International Conference on Micro Electro Mechanical Systems, Hong Kong, Jan. 24-28:352–355
3. Myers DR, Cheng KB, Jamshidi B, Azevedo RG, Senesky DG, Wijesundara MBJ Pisano AP (2009). A Silicon Carbide Resonant Tuning Fork for Micro-Sensing Applications in High Temperature and High G-Shock Environment. Journal of Micro/Nanolithography, MEMS, and MOEMS 8:021116
4. Suster M, Guo J, Chaimanonart N, Ko WH, Young DJ (2006). A High-Performance MEMS Capacitive Strain Sensing Microsystem. JMEMS 15(5):1069–1077
5. Hetherington DL, Sniegowski JJ (1998). Improved Polysilicon Surface-micromachined Micromirror Devices using Chemical-mechanical Polishing. SPIE's 43rd Annual Meeting, San Diego, CA, July 22, 1998.
6. Fu XA, Dunning J, Zorman CA, Mehregany M (2005). Polycrystalline 3C-SiC thin films deposited by dual precursor LPCVD for MEMS applications. Sensors and Actuators A 119:169–176
7. Rogacheva NN (2004). The Theory of Piezoelectric Shells and Plates. CRC Press.
8. Toriyama T (2004). Piezoresistance Consideration on n-type 6H SiC for MEMS-based Piezoresistance Sensors. J. Micromech. Microeng. 14:1445–1448
9. Azevedo RG, Chen I-Y, OŔeilly OM, Pisano AP (2005). Influence of Sensor Substrate Geometry on the Sensitivity of MEMS Micro-extensometers. IMECE Orlando, FL:IMECE2005-82724
10. MicroStrain, Inc. USA. http://microstrain.com
11. Beckwith TG, Marangoni RD, Lienhard JH (1993). Mechanical Measurements. Addison-Wesley, 5th Ed.
12. Jamshidi B, Azevedo RG, Wijesundara MBJ, Pisano AP (2007). Corrosion Enhanced Capacitive Strain Gauge at 370C. MEMS 2007, 20th IEEE SENSORS 2007 Conference on Micro and Nano sensors Technical Digest 2007:804–807
13. Tongue BH (2001). Principles of Vibration. Oxford University Press, 2nd Ed.
14. Azevedo RG, Zhang J, Jones DG, Myers DR, Jog AV, Jamshidi B, Wijesundara MBJ, Maboudian R, Pisano AP (2007). Silicon Carbide Coated MEMS Strain Sensor for Harsh Environment Applications, MEMS 2007, 20th IEEE International Conference on Micro Electro Mechanical Systems, Technical Digest 2007:643–646
15. Azevedo RG, Jones DG, Jog AV, Jamshidi B, Myers DR, Chen L, Fu, XA, Mehregany, M, Wijesundara, MBJ, Pisano, AP (2007). A SiC MEMS Resonant Strain Sensor for Harsh Environment Applications, IEEE Sensors, 7(4):568–576
16. Wojciechowski KE, Boser BE, Pisano AP (2004). A MEMS resonant strain sensor operated in air. MEMS Conference 2004: 841–845
17. Krauthammer T, Venstal E (2001). Thin Plates and Shells: Theory, Analysis, and Applications. CRC Press.
18. Di Giovanni M (1982). Flat and Corrugated Diaphragm Design Handbook. CRC Press.
19. Beeby S (2004). MEMS Mechanical Sensors. Artech.
20. Zeirmann R, von Berg J, Reichert W, Obermeier E, Eickhoff M, Krotz G (1997). A high temperature pressure sensor with β-SiC on SOI substrates. Int. Conf. Solid State Sensors and Actuators, Chicago, June 16-19:1411–1414
21. Okojie R, Ned A, Kurtz A (1997). Operation of 6H-SiC Pressure Sensor at 500 °C. Tech. Dig. 1997 Int. Conf. Solid State Sensors and Actuators,Chicago IL, June 1619:1407-1409
22. Eickhoff M, Möller H, Krotez G, Berg JV, Ziermann R (1999). A High Temperature Pressure Sensor Prepared by Selective Deposition of Cubic Silicon Carbide on SOI Substrates. Sensors and Actuators A 74:56–59

23. Faris W, Mohammed H (2004). A comparison between two solution approaches for diaphragm-based capacitive pressure microsensor. ICSE Dec 7-9:295–297
24. Pakula LS, Yang H, Pham HTM, French PJ, Sarro PM (2004). Fabrication of a CMOS compatible pressure sensor for harsh environments. J. Micromech. and Microeng. 14(11):1478–1483
25. Young DJ, Du J, Zorman CA, Ko WH (2004). High-Temperature Single-Crystal 3C-SiC Capacitive Pressure Sensor. IEEE Sensors Journal 4(4):464–470
26. Chen L, Mehregany M (2008). A silicon carbide capacitive pressure sensor for in-cylinder pressure measurement. Sensors and Actuators A 145146:2-8
27. Seshia AA, Palaniapan M, Roessig TA, Howe RT, Gooch RW, Schimert TR, Montague S (2002). A vacuum packaged surface micromachined resonant accelerometer. JMEMS 11(6):784–793
28. Atwell AR, Okokie RS, Kornegay KT, Roberson SL, Beliveau A (2003). Simulation, fabrication and testing of bulk micromachined 6H-SiC high-g piezoresistive accelerometers. Sensors and Acutators A 104:11–18
29. Rajgopal S, Zula D, Garverick S, Mehregany M (2009). A Silicon Carbide Accelerometer for Extreme Environment Applications. Materials Science Forum 600-603:859–862
30. Pakula LS, Yang H, French PJ (2003). A CMOS compatible SiC accelerometer. Sensors 2003:761–764
31. Fleischman AJ, Roy S, Zorman CA, Mehregany M (1996). Polycrystalline silicon carbide for surface micromachining. MEMS 1996, San Diego, Feb. 11-15:234-238
32. Fleischman AJ, Roy S, Zorman CA, Mehregany M (1997). Behavior of polycrystalline SiC and Si surface-micromachined lateral resonant structures at elevated temperatures. Int. Conf. Silicon Carbide, IIINitrides, and Related Materials, Stockholm, Aug. 31-Sept. 5:643–644
33. Wiser R, Zorman ZA, Mehregany M (2003). Fabrication and testing of vertically-actuated polycrystalline silicon carbide micromechanical resonators for MHz frequency applications. Transducers 2003, Boston, June 8-12:1164–1167
34. Bhave SA, Gao D, Maboudian R, Howe RT (2005). Fully-differentical poly-SiC lame-mode resonator and checkerboard filter. MEMS 2005, 18th IEEE International Conference on Micro Electro Mechanical Systems, Technical Digest (2005):223–226
35. Jiang L, Cheung R, Hedley J, Hassan M, Harris AJ, Burdess JS, Mehregany M, Zorman CA (2006). SiC cantilever resonators with electrothermal actuation. Sensors and Actuators A 128:376–386
36. Seshia AA, Howe RT, Montague S (2002). A Micromechanical Resonant Output Gyroscope. Proc. IEEE MEMS 2002, Las Vegas, Jan. 20-24:722–727
37. Xie H, Fedder GK (2003). Fabrication, Characterization, and Analysis of a DRIE CMOS-MEMS Gyroscope. IEEE Sensors Journal 3(5):622–631
38. Maenaka K, Ioku S, Fujita T, Takayama Y (2005). Design, fabrication and operation of MEMS gimbal gyroscope. Sensors and Actuators A 121(1):6–15
39. Cheung R (ed.) (2006). Silicon Carbide Micro Electromechanical Systems. Imperial College Press.
40. Lloyd Spetz A, Baranzahi A, Tobias P, Lundström I (1997). High temperature sensors based on metal-insulator-silicon carbide devices. Phys. Stat. Sol. A 162:493–511
41. Baranzahi A, Lloyd Spetz A, Glavmo M, Carlsson C, Nytomt J, Salomonsson P, Jobson E, Häggendal B, Martensson P, Lundström I (1997). Response of metal-oxide-silicon carbide sensors to simulated and real exhaust gases. Sensors and Actuators B 43:52–59
42. Moritz W, Fillipov V, Vasiliev A, Terentjev A (1999). Silicon carbide based semiconductor sensor for the detection of fluorocarbons. Sensors and Actuators B 58:486–490
43. Svennigstorp H, Widén B, Salomonsson P, Ekedahl L-G, Lundström I, Tobias P, Lloyd Spetz A (2001). Detection of HC in exhaust gases by an array of MISiC sensors. Sensors and Actuators B 77:177–185
44. Wright NG, Horsfall AB (2007). SiC sensors: a review. J. Phys. D: Appl. Phys. 40:6345–6354
45. Wiche G, Berns A, Steffes H, Obermeier E (2005). Thermal analysis of silicon carbide based micro hotplates for metal oxide gas sensors. Sensors and Actuators A 123-124:12–17

46. Cree Inc., USA. http://www.cree.com
47. Zhu H, Chen X, Cai J, Wu Z (2009). 4HSiC ultraviolet avalanche photodetectors with low breakdown voltage and high gain. Solid-State Electronics 53(1):7–10
48. Torvik JT, Pankove JI, Van Zeghbroeck BJ (1999). IEEE Trans. Electron Devices 46(7):1326–1331
49. Seely JF, Kjorntattanawanich B, Holland GE, Korde R (2005). Response of a SiC photodiode to extreme ultraviolet through visible radiation. Optics Letters 30(23):3120–3122
50. Strokan NB, Ivanov AM, Savkina NS, Streichuk AM, Lebedev AA, Syväjärvi M, Yakimova R (2003). Detection of strongly and weakly ionizing radiation by triode structure based on SiC films. J. Appl. Phys. 93:5714–5719
51. Nagai T, Yamamoto K, Kobayashi I (1982). SiC thin-film thermistor. J. Phys. E: Sci. Instrum. 15:520–524
52. de Vasconcelos EA, Khan SA, Zhang WY, Uchida H, Katsube T (2000). Highly sensitive thermistors based on high-purity polycrystalline cubic silicon carbide. Sensors and Actuators 83:167–171
53. Kiewra EW, Wayner Jr PC (1989). The Development of a Thin-Film Silicon Carbide Thermistor Array for Determining Temperature Profiles in an Evaporating Liquid Film. J. Electrochem. Soc. 136(3):740–744
54. Casady JB, Dillard WC, Johnson RW, Rao U (1996). A Hybrid 6H-SiC Temperature Sensor Operational from 25 °C to 500 °C. IEEE Trans. Comp., Pack., Manuf. Tech. A 19(3):416–422
55. Casady JB, Johnson RW (1996). Status of Silicon Carbide (SiC) as a Wide-Bandgap Semiconductor for High-Temperature Applications: A Review. Solid-State Electronics 39(10):1409–1422
56. Riza NA, Sheikh M (2010). Silicon Carbide-Based Extreme Environment Hybrid Design Temperature Sensor Using Optical Pyrometry and Laser Interferometry. IEEE Sensors Journal 10(2):219–224
57. Slack GA (1975). Thermal expansion of some diamondlike crystals. J. Applied Physics 46(1):89–98
58. Reeber RR, Wang K (1996) Thermal expansion and lattice parameters of group IV semiconductors. Materials Chemistry and Physics 46:259-264
59. Reeber RR, Wang K (1996) Thermal expansion of β-SiC, GaP and InP. Materials Research Symposium Proceedings 410:211-216
60. Azevedo RG, Myers DR, Pisano AP (2009). Temperature-insensitive silicon carbide resonant micro-extensometers. Transducers 2009, Denver, June 21-25:268–271
61. Berry BS, Pritchett WC, Fuentes RI, Babich I (1991). Stress and thermal expansion of β-SiC films by the vibrating-membrane method. J. Mater. Res. 6(5):1061–1065
62. Okojie RS (2004). Inelastic Stress Relaxation in Single Crystal SiC Substrates. Material Science Forum 457-460:375–378
63. Zhang J, Howe RT, Maboudian R (2006). Control of strain gradient in doped polycrystalline silicon carbide films through tailored doping. J. Micromech. Microeng. 16:L1-L5
64. Roessig TA, Howe RT, Pisano AP, Smith JH (2007). Surface-micromachined resonant accelerometer. 1997 International Conference on Solid-State Sensors and Actuators:859–862
65. Srikar VT, Senturia SD (2001). The design and analysis of shock resistant microsystems (MEMS). Transducers 2001, Munich, Germany:1370–1373